

博士論文(要約)

Doctoral Dissertation (Censored)

**Chemistry of cryovolcanism on Ceres  
and other icy bodies**

(Ceres および他の氷天体における低温火山の化学的研究)

A Dissertation Submitted for the Degree of Doctor of Philosophy  
December 2021

令和3年12月博士(理学)申請

Department of Earth and Planetary Science,  
Graduate School of Science, The University of Tokyo  
東京大学大学院理学系研究科 地球惑星科学専攻

Masahiro Yoda

依田 優大

## Abstract

Ceres is a dwarf planet in the asteroid belt, which have been attracting attention due to the possibility of liquid eruption from the interior, namely, cryovolcanism. The surface of Ceres typically comprises dark components, such as organic matter, and several secondary minerals, such as serpentine,  $\text{NH}_4$ -bearing phyllosilicate, and Mg carbonate. In addition to the secondary minerals, the bright materials mainly composed of  $\text{Na}_2\text{CO}_3$  with small amounts of  $\text{NH}_4$ -bearing salts have been observed on Ceres, especially on geologically young craters, such as the Occator crater. Gravity and geomorphic data strongly suggest that upwelling of deep subsurface oceanic water from the uppermost layer of the inner core would have occurred upon an impact. On the other hand, the presence of  $\text{Na}_2\text{CO}_3$  in the bright materials requires highly alkaline brines (e.g.,  $\text{pH} > 11$ ) as the source of cryovolcanism, although water chemistry of deep oceanic water is suggested to be moderately alkaline (e.g.,  $9 < \text{pH} < 10.5$ ) given the water-rock interactions on Ceres. Thereby, there was a contradiction between geophysical (gravity and geomorphology) evidence and geochemical prediction for formation of the bright materials on Ceres.

One potential issue in the previous studies is that effects of decompression of liquid brines upon eruption on salt formation are unclear. Previous studies investigated salt formation from brines using thermodynamic equilibrium model or in laboratory experiments, in which freezing rate of brines was changed. However, there is no experimental study examining salt formation during rapid decompression upon eruption. Degassing of volatile gas species caused by rapid decompression would change the pH of liquid brine and thus should affect salt precipitation. Another potential issue in previous studies concerns the aqueous chemical evolution of freezing subsurface brines. Although liquid brines would have been erupted from shallow subsurface brine reservoirs that were formed by upwelling deep oceanic water, the aqueous chemistry in freezing brine reservoir had not been evaluated due to lack of investigations and models for the compositional change of freezing alkaline brines.

In this thesis, we examined the salt formation upon decompression of liquid brines by laboratory experiments (Chapter 2). In the experiments, we focused on whether

$\text{Na}_2\text{CO}_3$ -rich salts can precipitate from brines with moderately alkaline pH ( $9 < \text{pH} < 10.5$ ) and volatiles of  $\text{CO}_2$  and  $\text{NH}_3$ , which was suggested for subsurface liquid brine in Ceres. We found that explosive bubbling and disruption of brines in rapid decompression was driven by degassing of  $\text{CO}_2$ . The effective degassing of  $\text{CO}_2$  in turn would have resulted in rapid alkalization of brines during decompression. Owing to the alkalization upon rapid decompression,  $\text{Na}_2\text{CO}_3$ -rich salts can be formed from moderately alkaline brines (e.g., pH down to 10.0) with low  $\text{NH}_3/\text{CO}_2$  ratios. In addition to  $\text{Na}_2\text{CO}_3$ -rich salts,  $\text{NH}_4$ -bearing salts ( $\text{NH}_4\text{HCO}_3$ ) were also formed if the brine samples contain the highly levels of  $\text{NH}_3$  ( $\Sigma\text{NH}_3/\Sigma\text{CO}_2 \sim 1$ ). Based on the results, we constrained the possible chemical compositions of subsurface brine reservoirs as explanations of the both  $\text{Na}_2\text{CO}_3$ -rich salts and  $\text{NH}_4$ -bearing salts in the bright materials on Ceres.

As for the evaluation of aqueous chemistry in freezing subsurface liquid brines, the field investigations for freezing alkaline saline lakes in Mongolia were undertaken for terrestrial analogs (Chapter 3). We analyzed the abundance and mineral compositions of salts entrapped in overlying lake ice as well as water chemistry of bottom lake water. Using a combination of mass balance calculation and aqueous geochemical modeling, we reproduced the general trend of ice salinity due to entrapment of lake water upon freezing and lake bottom-water observed by field investigations.

Finally, in Chapter 4, we calculate the chemical evolution of freezing subsurface brine reservoirs for various starting deep subsurface oceanic water compositions on Ceres using the model developed in Chapter 3. Results of the chemical evolution tracks of freezing brines are compared with the conditions of precipitation of both  $\text{Na}_2\text{CO}_3$ -rich salt and  $\text{NH}_4$ -bearing salts through rapid decompression revealed in Chapter 2. The comparison suggests that if the subsurface liquid brines originate from deep oceanic water generated by water-rock interactions with water-to-rock ratios of 0.4–1.1, both  $\text{Na}_2\text{CO}_3$ -rich salts and  $\text{NH}_4$ -bearing salts in the bright materials can be explained. The constrained range of water-to-rock ratios matches that of the inner core of Ceres based on the mean moment of inertia. Our results suggest that by taking into account both degassing of volatiles in cryovolcanic eruption and chemical evolution during freezing of brine reservoirs, the geophysical evidence of upwelling deep subsurface oceanic water and geochemical evidence of the presence of  $\text{Na}_2\text{CO}_3$ -rich salts and  $\text{NH}_4$ -bearing salts can be explained consistently. Considering the young surface age of the bright materials, our results support that Ceres may have maintained the deep subsurface liquid ocean within the entire of the inner core until today. Detailed explorations of the bright materials through remote-sensing and in-situ analyses would be an important target to reveal the nature of the prolonged ocean on Ceres in future missions and astrobiology.

## Acknowledgements

My deepest appreciation goes to Prof. Y. Sekine for his continuous encouragement to this challenging theme. Without his thoughtful and kind supports, I could not achieve this work.

I gratefully acknowledge Prof. K. Fukushi in Kanazawa University for organization of field investigations, proposal for Joint research program and kind supports in research life in doctor course. I sincerely thank Mr. T. Kitajima, Ms. B. Gankhurel and S. Ganbat of Kanazawa University for support in field investigations and sample analysis of field investigations in Mongolia. I appreciate for D. Davaasuren and T. Gerelmaa in University of Mongolia about the organization of field investigations. I also appreciate for Dr. D. Shoji and Prof. M. Zolotov both useful comments and providing the geochemical model. I would like to thank Prof. Y. Takahashi for useful comments and kind supports in the chemical analyses. I would like to thank Dr. T. Shibuya and Dr. S. Kikuchi in JAMSTEC for numerical simulations on geochemical modeling. I also appreciate the suggestions provided from Dr. S. Tan and Dr. H. Kurokawa in ELSI about geochemical modeling. I would like to thank Prof. A. Kano, Prof. S. Sugita, and Prof. K. Goto for their critical reviews and helpful comments. I would like to thank Prof. H. Kayane, Prof. S. Tachibana, Assoc. Prof. A. Takigawa, Assoc. Prof. M. Ikeda, Dr. S. Takahashi, Dr. H. Kawahara, and Dr. N. Motegi. Their comments and advice help this study in seminars. I am grateful to Assoc. Prof. H. Genda, Dr. K. Hamano, Dr. K. Sugiura, Dr. Y. Endo and Dr. N. Zhang for a lot of comments and suggestions in the seminars at ELSI.

In my doctor course, I had been encouraged by H. Tabata, N. Noda, S. Imamura, E. Hirai, H. Shozaki, M. Sugiuchi, K. Kaneko, P. Prondzinsky, F. Li-Hau, J. Anderson and T. Fukuhata for their help to write this thesis. I wish to express my sincere thanks to Prof. K. Kurita, Prof. E. Tajika and Dr. R. Noguchi for kindly encouragements throughout my master and doctor course. I also appreciate for ex-colleagues in Sumitomo Mitsui Trust Bank. Finally, I would also like to express my appreciation to my family for their supports and warm encouragements.

# Contents

Abstract.....	I
Acknowledgements .....	III
Chapter 1. General Introduction .....	1
1.1 Potential for cryovolcanism on Ceres ...エラー! ブックマークが定義されていません。	
1.2 Formation of bright material on Ceres ..エラー! ブックマークが定義されていません。	
1.3 Potential issues .....	エラー! ブックマークが定義されていません。
1.4 Thesis overview and objectives....	エラー! ブックマークが定義されていません。
Chapter 2. Effects of decompression of Na-bearing alkaline brines on precipitation of Na carbonates: Implications for formation of bright materials by cryovolcanic eruption on Ceres .....	13
2.1 Objectives and overview of Chapter 2 ..エラー! ブックマークが定義されていません。	
2.2 Experimental setup .....	エラー! ブックマークが定義されていません。
2.2.1 Experimental system.....	エラー! ブックマークが定義されていません。
2.2.2 Brine samples.....	エラー! ブックマークが定義されていません。
2.2.3 Decompression.....	エラー! ブックマークが定義されていません。
2.2.4 Analysis of salt samples .....	エラー! ブックマークが定義されていません。
2.3 Results of decompression experiments .エラー! ブックマークが定義されていません。	
2.3.1 Dynamic behaviors of brines with decompression. エラー! ブックマークが定義されていません。	
2.3.1.1 Slow decompression .....	エラー! ブックマークが定義されていません。
2.3.1.2 Rapid decompression .....	エラー! ブックマークが定義されていません。
2.3.2 Mineral composition of salts .....	エラー! ブックマークが定義されていません。
2.3.2.1 Na carbonate formation upon decompression	エラー! ブックマークが定義されていません。
2.3.2.2 Effects of NH <sub>3</sub> on Na carbonate formation. エラー! ブックマークが定義されていません。	

- 2.4 Discussion on salts formation upon decompression experiments エラー! ブックマークが定義されていません。
- 2.4.1 Thermodynamic equilibrium calculations..... エラー! ブックマークが定義されていません。
- 2.4.2 Mechanism of Na carbonate formation in rapid decompression エラー! ブックマークが定義されていません。
- 2.5 Implications for bright materials and subsurface brines on Ceres エラー! ブックマークが定義されていません。
- 2.5.1 Uncertainties in our experiments toward applications to Ceres.. エラー! ブックマークが定義されていません。
- 2.5.2 Implications for interpretations for bright materials on Ceres エラー! ブックマークが定義されていません。
- 2.6 Summary of Chapter 2 ..... エラー! ブックマークが定義されていません。

Chapter 3. Field investigations and model interpretation of aqueous chemistry in freezing closed-basin lakes of Mongolia as analogs of subsurface brines on icy bodies ..... 59

3.1 Objectives and overview of Chapter 3 .....60

3.2 Study area and methodology .....61

3.2.1 Geohydrological setting ..... 61

3.2.2 Sampling ..... 63

3.2.3 Sample analyses ..... 65

3.3 Results and discussion of field surveys .....68

3.3.1 Surface morphology of ice-covered saline lakes ..... 68

3.3.2 Salinity trapped in ice ..... 69

3.3.3 Chemical compositions of the ice and bottom-water ..... 70

3.3.4 Mineralogy of the solid residues in ice ..... 71

3.4 Model calculations of the aqueous evolution in freezing saline lakes of Mongolia ....78

3.4.1 Model description..... 78

3.4.2 Model parameters..... 79

3.4.3 Model results ..... 84

3.5 Interpretations of chemical partitioning based on model calculations and field observations.....88

3.5.1 Olgoy Lake..... 88

3.6.2	Orog Lake.....	91
3.6	Implications for subsurface brine reservoir on icy bodies .....	92
3.7	Summary of Chapter 3 .....	94

## Chapter 4. Chemical evolution of subsurface brines and formation of bright materials on Ceres ..... 95

4.1	Objectives and overview of Chapter 4 ..エラー! ブックマークが定義されていません。	
4.2	Deep subsurface oceanic water on Ceres.. エラー! ブックマークが定義されていません。	
4.3	Modeling of chemical evolution of brine reservoirs .エラー! ブックマークが定義されていません。	
4.3.1	Model parameters and settings.....エラー! ブックマークが定義されていません。	
4.3.2	Modeling results of chemical evolution of freezing brine reservoirs .エラー! ブックマークが定義されていません。	
4.4	Chemical evolution of subsurface brines and salt formation upon its eruption on Ceres エラー! ブックマークが定義されていません。	
4.5	Uncertainties and unknown factors in the model . エラー! ブックマークが定義されていません。	
4.6	Implications for the subsurface ocean and thermal history on Ceres エラー! ブックマークが定義されていません。	
4.7	Summary of Chapter 4 ..... エラー! ブックマークが定義されていません。	

Chapter 5. General Conclusions .....	117
5.1 New findings of this thesis provided from experiments and modeling.エラー! ブック マークが定義されていません。	
5.2 Future perspectives for Ceres and other icy bodies. .エラー! ブックマークが定義さ れていません。	
References .....	123
Appendix A.....	131

## **Chapter 1. General Introduction**

本章については、五年以内に雑誌等で刊行予定のため、非公開。

## **Chapter 2. Effects of decompression of Na-bearing alkaline brines on precipitation of Na carbonates: Implications for formation of bright materials by cryovolcanic eruption on Ceres**

本章については、五年以内に雑誌等で刊行予定のため、非公開。

**Chapter 3. Field investigations and model interpretation of aqueous chemistry in freezing closed-basin lakes of Mongolia as analogs of subsurface brines on icy bodies**

### 3.1 Objectives and overview of Chapter 3

Surface morphology and gravity data observed by the Dawn spacecraft strongly suggest the presence of shallow brine reservoirs beneath the bright materials on Ceres (e.g., Raymond et al., 2020). Similar shallow subsurface brine reservoirs are suggested to exist beneath geologically-young chaotic terrains of Europa (e.g., Head & Pappalardo, 1999). Small-scale lenticulae on Europa's chaotic terrains were likely formed by disruption of the surface ice layer through volume changes in the underlying shallow, subsurface brine reservoirs (e.g., Culha & Manga, 2016; Manga & Michaut, 2017). These shallow subsurface brines would have produced by temporal geological events, such as impact cratering and upwelling of high-temperature fluids from the subsurface oceans (e.g., Fagent, 2003; Pappalardo & Barr, 2004). Thus, the shallow brine reservoirs are considered to freeze due to loss of heat by conduction to surrounding low-temperature crust.

During freezing of shallow subsurface brine reservoirs, a part of brines could be trapped within pores of ice at the interface between a subsurface reservoir and overlying ice layer, which is analogous to trapping of seawater within sea ice on Earth (Head & Pappalardo, 1999; Zolotov & Kargel, 2009). Another process is the trapping of seawater within cracks that formed in an ice shell (Pappalardo & Barr, 2004). In addition, authigenic precipitations of salts could occur in response to concentrations of dissolved species in freezing brine reservoirs. Partitioning of salts into the ice layer and authigenic mineral precipitation cannot be investigated only using thermodynamic equilibrium models, because both processes could be controlled by kinetics. In the case of capture of seawater within sea ice on Earth, theoretical models have been developed based on both field investigations (e.g., Nakawo & Sinha, 1981) and laboratory experiments (e.g., Cox & Weeks, 1975; Weeks & Lofgren, 1967). Although there are a number of previous studies about pressure ridges in Earth's sea ice (e.g., Strub-Klein & Sudom, 2012), it is uncertain whether the knowledge is directly applicable to pressure-induced cracks on icy bodies because pressure ridge formation in Earth's ocean often occurs as an open system without fixed ends of floating ice sheet. In addition, the chemical composition of Earth's seawater does not change significantly with sea ice growth, whereas the chemical composition of a subsurface brine reservoir on icy bodies can change dramatically through time owing to the salinity increase and precipitation of authigenic minerals in response to freezing. Thus, the aqueous chemistry of freezing brine reservoirs cannot be examined solely through investigations of Earth's sea ice. Despite the importance of salt capturing processes within ice, there are, to our knowledge, no field investigations of

alkaline-saline lakes as their terrestrial analogs examining the chemical partitioning of dissolved ions and solid precipitates between a subsurface brine reservoir and overlying ice.

The aim of this chapter is to construct an aqueous geochemistry model that can treat compositional changes in freezing subsurface brine reservoirs aqueous based on factual evidence obtained in field surveys to freezing alkaline saline lakes (see Chapter 1). To this end, we investigated both the partitioning of salinity between a brine reservoir and overlying ice and the water chemistry of the remaining brine reservoir upon freezing, based on field surveys of ice-covered saline lakes in the Valley of the Gobi Lakes, Mongolia (Yoda et al., 2021). These are closed-basin lakes without any outlet rivers (Section 3.2). It has been suggested that the water chemistry and mineral precipitation in these lakes are terrestrial analogs of alkaline–carbonate ocean worlds, such as Enceladus and Ceres (Fukushi et al., 2020), although one difference would be the possible presence of dissolved  $\text{NH}_3$  in brine reservoirs on Ceres (De Sanctis et al., 2016; 2020b). During cold seasons, the surfaces of the lakes are completely frozen, and volume expansion of freezing lake water could pressurize the surface ice, possibly leading to crack formation. The salinity of the lake bottom-water could increase owing to ice growth during cold seasons. These factors suggest that the geology, aqueous chemistry, and mineralogy of the freezing closed-basin lakes could be terrestrial analogs of freezing subsurface brine reservoirs on icy bodies, such as Ceres.

In the field investigations, we undertook observations of surface features (e.g., cracks and ridges) and measured the spatial distributions of salt contents within lake ice (Section 3.3). The lake bottom-water beneath the ice was collected to examine the water chemistry (Section 3.3). The ice salinity observations were compared with model calculations based on mass balance and aqueous chemistry using the FREZCHEM software (Section 3.4 and Section 3.5). Based on these results, we detail the implications of our field investigations for icy bodies (Section 3.6). Finally, we summarize our study (Section 3.7). The supplemental information of results in field surveys and model evaluations were summarized in Appendix A. All data in Chapter 3 are also available in Yoda et al. (2021).

## **3.2 Study area and methodology**

### **3.2.1 Geohydrological setting**

The study area is located in the transition zone between the Gobi Desert and the Altai Mountain Range in southern–central Mongolia (Fig. 3.1). This area is called the

Valley of the Gobi Lakes, where several closed-basin lakes occur in a latitudinally oriented depression of tectonic origin between the Khangai and Gobi–Altai mountains (Fig. 3.1). In February 2019 and January 2020, we conducted field surveys of two closed-basin lakes in the Valley of the Gobi Lakes: Orog Lake (45°3'57"N, 100°34'22"E) and Olgoy Lake (46°33'48"N, 100°6'29"E; Figs. 3.2). The survey in February 2019 was preliminary because the sampling locations on the frozen lakes were limited, whereas the survey in January 2020 was the major survey, in which the sampling was conducted over large areas of the frozen lakes.

Orog Lake is located ~20 km south of the town of Bogd (Fig. 3.1). The elevation of Orog Lake is ~1220 m above sea level. Orog Lake is fed by the Tuin River, which originates in the Khangai Mountains (Fig. 3.1). The Tuin River flows through proluvial regions of dry steppe and feeds into the eastern side of Orog Lake in the semiarid climate zone (Szumińska, 2016; Sekine et al., 2020) (Figs. 3.2a). The surface area of Orog Lake is ~140 km<sup>2</sup>, and it has a maximum depth of 1–3 m (Davaa et al., 2007). Orog Lake can be divided into three sub-lakes: eastern, central, and western (Fig. 3.2a). These three sub-lakes are connected through shallow neck regions during warm seasons (Fig. 3.2a). Tuin River flows into the central and eastern parts of Orog Lake (Fig. 3.2a).

Olgoy Lake is located ~60 km west of the city of Bayankhongor (Fig. 3.1). The elevation of Olgoy Lake is ~2100 m above sea level, and it is an oxbow lake of the nearby Sumber River (Fig. 3.2b). This lake is one of the closed-basin lakes developed in a local depression in the southwestern Khangai Mountains (Fig. 3.1). The surface area of Olgoy Lake is ~1.5 km<sup>2</sup>, with a maximum depth of ~1 m.

In the Valley of the Gobi Lakes, the annual mean precipitation is 50–100 mm. The precipitation occurs mainly from the April to October. The other seasons are generally dry, with precipitation of <5 mm/month (e.g., Davaa et al., 2007). The aridity index, which is defined as the ratio of precipitation to potential evaporation, is about 0.2–0.3 in the Valley of the Gobi Lakes (Davaa et al., 2007). The annual mean air temperature around Orog Lake is ~1 °C (Szumińska, 2016). In Olgoy and Orog lakes, the daily mean air temperature typically decreases to ~0 °C or less from October or November, which results in freezing of the lake surface. In January and February, the daily mean maximum and minimum temperatures were about –5 to –10 °C and –20 to –25 °C, respectively (i.e., in Bayankhongor). The air temperature around Olgoy Lake is typically 4–5 °C lower than that around Orog Lake due to its higher elevation. The meteorological data show that daily air temperatures were <0 °C during January and February, indicating that the surface ice of Orog and Olgoy lakes experienced no melting. Given the salinity levels of the Orog and Olgoy lakes (a few ‰), the freezing point depression of the lake water is less than –

1 °C. The precipitation data suggest that inputs of snow to the surface ice of the lakes was negligible (<10 mm) compared with the ice thickness (~1 m).

Our previous study investigated the hydrology around Orog and Olgoy lakes through field surveys in warm seasons (Sekine et al., 2020). Based on this previous study, the major water source of Orog Lake during summer is the Tuin River, along with underground water flow along the river and local springs (Sekine et al., 2020). In the surveys of the present study, the surface of Tuin River was completely frozen. However, we found that a small input of underground water occurs along the river into the central Orog Lake, even in February. The major water source of Olgoy Lake during summer is local springs, which originates melting of permafrost (Sekine et al., 2020). In the surveys of February 2019 and January 2020, we recorded no significant inputs of spring water into Olgoy Lake due to the low temperatures (−20 °C).

Table A1 in Appendix A lists the dissolved species, alkalinity, and pH of the water of both lakes in summer 2018. Both lake waters have salinity of 1-2 g/kg and pH of 9–10 (Fukushi et al., 2020). The lake waters are sodium bicarbonate type, which means that  $\text{Na}^+$  and  $\text{HCO}_3^-$  are the major cation and anion, respectively (Sekine et al., 2020). In addition, the concentrations of  $\text{Cl}^-$  and  $\text{Mg}^{2+}$  are substantial in Orog and Olgoy lakes, respectively. The central part of Orog Lake has lower concentrations of dissolved species than its western part (Table A1 in Appendix A). This is because the lake water in the central part is diluted by less saline water from Tuin River and underground sources (Fig. 3.2a).

In Orog and Olgoy lakes, the hyposaline and alkaline lake waters are the result of evaporative concentration of the lake water and accumulation of conservative  $\text{Na}^+$  (and  $\text{Cl}^-$ ) in the lakes in the semiarid climate and in the absence of any outlet rivers (Sekine et al., 2020). Under these alkaline conditions, authigenic precipitation of carbonate minerals, such as monohydrocalcite (MHC;  $\text{CaCO}_3 \cdot \text{H}_2\text{O}$ ), occurs in the water column of the lakes (Fukushi et al., 2020; Fukushi & Matsumiya, 2018). The calculated near-zero saturation index of MHC for the measured  $\text{Ca}^{2+}$  and alkalinity of Orog Lake suggests that the lake water is saturated with MHC during the summer (Table A1 in Appendix A). In contrast, chlorides (e.g.,  $\text{NaCl}$ ) and sulfates (e.g.,  $\text{Na}_2\text{SO}_4$ ) are undersaturated in both lakes during the summer (Table A1 in Appendix A).

### 3.2.2 Sampling

In the field surveys of January 2020 and February 2019, the surfaces of both Orog and Olgoy lakes were covered with ice with a thickness of 60–100 cm. Given that the lakes started to freeze from October (Section 3.2.1), the mean growth rate of the

surface ice would be  $\sim 1 \times 10^{-5}$  cm/s, assuming a constant growth rate. In both lakes, bottom-waters were present below the surface ice at some locations during the surveys (Fig. 3.3a).

Figure 3.2 shows the locations of the sampling sites. Table A2 in Appendix A lists the latitudes and longitudes, sampling depths of ice, bottom-water thickness, ice thickness, and sampling dates of the sampled sites. The field observations were performed on-site and from the air by taking aerial photographs using a drone (DJI Phantom 4 Pro). The ice samples were collected using a hand drill with a diameter of 15 cm. Crushed ice flakes generated by drilling were collected at different depths from the surface (Table A2 in Appendix A). After collecting sample at one depth, we removed remnant of crushed ice flakes in the drill hole by hands as much as possible before drilling to different depths. We collected the ice samples at nine sampling sites in Orog Lake (four from the western part and five from the central part; Fig. 3.2a), and at six sampling sites in Olgoy Lake (Fig. 3.2b). One hole was drilled at each sampling site, except for sites Orog\_2020W2 and Olgoy\_2020C1 (Fig. 3.2). At Orog\_2020W2 and Olgoy\_2020C1, two and three drill holes were drilled, respectively, to collect samples with and without cracks on the surface (Fig. 3.2). The ice samples were stored in pre-cleaned plastic bottles with a volume of 50 mL for chemical analysis of the saline materials captured in the ice, and in plastic bags with a volume of 3 L for the mineralogical analysis of the solid residues after freeze-drying of the ice samples (Section 3.2.3).

After thawing the ice samples in the plastic bottles, they were filtered with a 0.45  $\mu\text{m}$  membrane (ADVANTEC Inc.) to remove aeolian dust. This process also removed precipitated authigenic minerals in the water column. The filtered solutions were used to measure the total abundances of dissolved  $\text{Na}^+$ ,  $\text{K}^+$ ,  $\text{Mg}^{2+}$ ,  $\text{Ca}^{2+}$ ,  $\text{Cl}^-$ , and  $\text{SO}_4^{2-}$  in the ice (Section 3.2.3). We obtained the total salinity by summing the measured abundances of dissolved elements in the samples. We did not measure pH and dissolved carbonates ( $\text{HCO}_3^-$  and  $\text{CO}_3^{2-}$ ) in the thawed ice samples because the original pH and amounts of dissolved carbonates would not be preserved due to exchange with  $\text{CO}_2$  in the atmosphere after thawing. Instead of measuring dissolved carbonates, we approximately estimated the alkalinity ( $= [\text{HCO}_3^-] + 2[\text{CO}_3^{2-}]$  (mEq/L), where  $[X]$  denotes the mmol/L of species X) in the ice samples based on the charge balance equation ( $[\text{Na}^+] + [\text{K}^+] + 2[\text{Mg}^{2+}] + 2[\text{Ca}^{2+}] = [\text{Cl}^-] + 2[\text{SO}_4^{2-}] + [\text{HCO}_3^-] + 2[\text{CO}_3^{2-}]$ ), assuming that contributions of other ions (e.g.,  $\text{H}^+$  and  $\text{OH}^-$ ) were negligible in the charge balance. Although we estimated the approximate alkalinity in the ice samples, we cannot estimate individual values of  $[\text{HCO}_3^-]$  and  $[\text{CO}_3^{2-}]$  because the original pH of the ice sample was unknown. Thereby, we did not include  $\text{HCO}_3^-$  and  $\text{CO}_3^{2-}$  into the salinity of the ice samples.

The ice samples in the plastic bags were kept frozen during the surveys, and were then freeze-dried using a vacuum freeze-dryer (FDU-1200; EYELA, Inc.) in a laboratory at the National University of Mongolia, Ulaanbaatar, Mongolia. The ice samples in the plastic bags were weighed before and after freeze-drying using a balance (Sartorius AG; BP102S Inc.). The freeze-dried solid residues were used to determine the solid phase compositions in the ice samples (Section 3.2.3).

When the drill reached bottom-waters, lake water, if present, overflowed onto the surface (Table A2 in Appendix A). We measured the dissolved O<sub>2</sub> (DO) levels, electric conductivity (EC), oxidation–reduction potential (ORP), pH, alkalinity, and temperature of the bottom-waters on-site. For EC, pH, and ORP, we used EC, pH, and ORP meters with electrodes (portable electrical conductivity pH meters; WM-32EP; TOA-DKK Corp., Tokyo, Japan). The pH electrode was calibrated using three pH buffer solutions (pH = 4.01, 6.86, and 9.18 at 25 °C) prior to the measurements. The DO concentrations were measured with a DO meter on-site (DO-31-3IP; TOA-DKK Corp., Tokyo, Japan). The measured DO values were corrected for the atmospheric pressure of each lake corresponding to the local elevations. After filtering using a 0.45 µm membrane, alkalinity was measured on-site for the water samples by titration with H<sub>2</sub>SO<sub>4</sub> solutions. The collected water samples were stored in two pre-cleaned plastic bottles with volumes of 100 mL after filtering with a 0.45 µm membrane (ADVANTEC Inc.) on-site.

### 3.2.3 Sample analyses

We measured the abundances of major cations (Na<sup>+</sup>, K<sup>+</sup>, Mg<sup>2+</sup>, and Ca<sup>2+</sup>) in the solution samples (i.e., thawed ice and lake bottom-water samples) using an inductively coupled plasma optical emission spectrometer (ICP–OES; ES-710S; Varian Inc.) at Kanazawa University, Kanazawa, Japan. The abundances of the major anions (Cl<sup>−</sup> and SO<sub>4</sub><sup>2−</sup>) were measured with an ion chromatograph (HPLC, 8020 series; Tosho Co. Inc.) at Kanazawa University. For the ICP–OES analyses, we added HNO<sub>3</sub> into the solution samples in order to produce 0.6% HNO<sub>3</sub> solutions to stabilize the cations.

After freeze-drying, the mineralogical compositions of the solid residues were determined with a X-ray diffraction (XRD) instrument (MiniFlex; Rigaku Corp. Ltd.) at Tokyo Institute of Technology, if the recovered amounts were sufficiently large. The scan range and step size were 5°–60° and 0.02°, respectively. The anode material was Cu in the XRD measurements. For solid residues with an insufficient amount for XRD analysis, X-ray absorption fine structure analysis (XAFS) was conducted to identify the mineralogy. The XAFS measurements were conducted on beamlines BL-9A and BL-19B at the Photon Factory, High Energy Accelerator Research Organization, KEK (Tukuba, Japan).

For the XAFS analyses, we placed the solid residues on conductive double-sided carbon tape attached to a stainless steel sample holder. The spectra were obtained in the X-ray fluorescence yield mode with a silicon drift detector under a high vacuum ( $\sim 1 \times 10^{-6}$  Pa). A solid state detector (SSD) was used to increase the detection sensitivity of beamline BL-9A. The REX2000 data analysis software package (Rigaku Co. Ltd.) was used for the analysis of the obtained spectra.

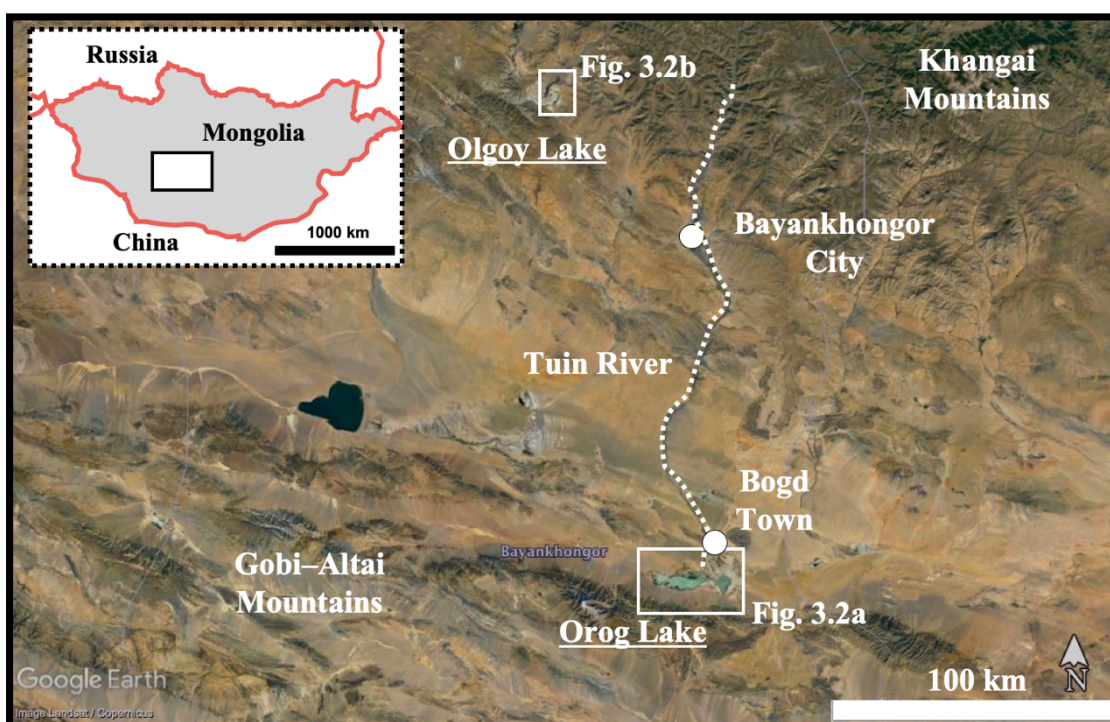


**Figure 3.1. Satellite image of the study area in Mongolia.** The upper left inset shows the location of Mongolia (the shaded region) and our study area (the black rectangle). The lower and upper white rectangles show the locations around Orog and Olgoi lakes, respectively. Close-up satellite images around the lakes are shown in Fig. 3.2. The dashed line shows Tuin River. White circles represent the locations of Bayankhongor and Bogd. The original image was taken from Google Earth.

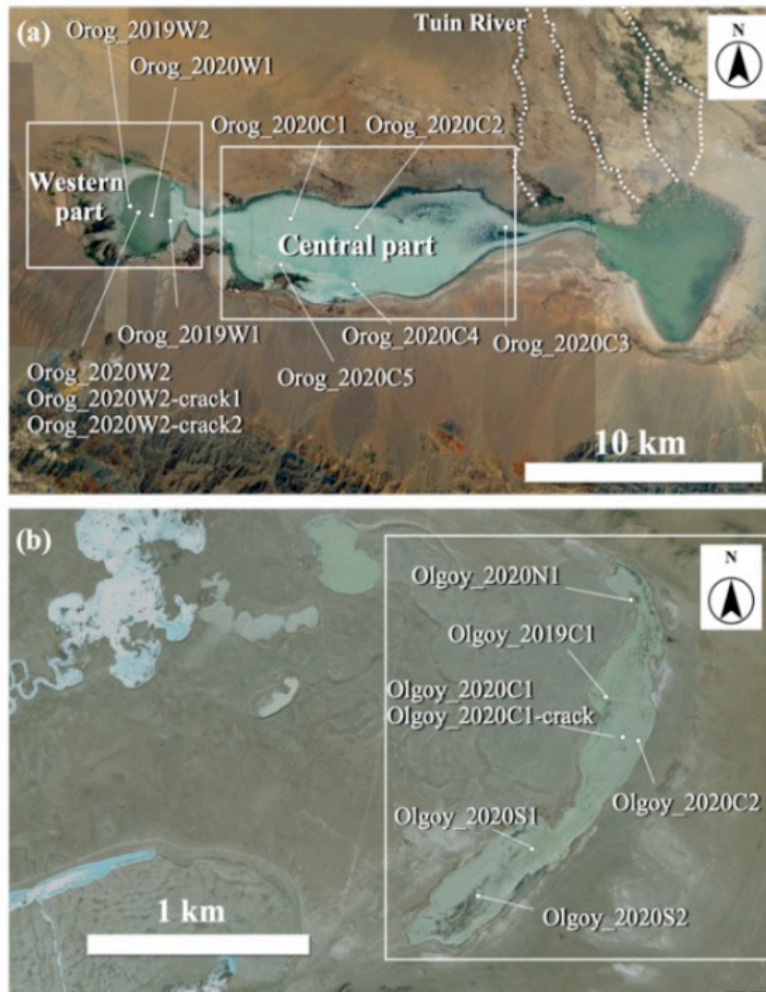


**Figure 3.2. Satellite images of Orog and Olgoy lakes.** The original images were taken from Google Earth. White dots represent the sampling locations in the January 2020 and February 2019 surveys, respectively. One hole was drilled at each sampling site, except for Orog\_2020W2 and Olgoy\_2020C1. At Orog\_2020W2, three holes were drilled for sampling, and two were on wet cracks (Orog\_2020W2-crack1 and Orog\_2020W2-crack2) and one was on the surface ice without wet cracks (Orog\_2020W2). At Olgoy\_2020C1, two holes were drilled, and one was on a contraction crack (Olgoy\_2020C1-crack) and the other was on the surface ice without cracks (Olgoy\_2020C1). (a) Satellite image of Orog Lake. White rectangles are the central and western parts of Orog Lake, respectively. Tuin River (i.e., the dashed line) flows into the eastern and central sub-lakes. (b) Satellite image of Olgoy Lake. Olgoy Lake is shown in the white rectangle.

### 3.3 Results and discussion of field surveys

#### 3.3.1 Surface morphology of ice-covered saline lakes

We found three types of cracks and fractures on Orog and Olgoy lakes in the field surveys: contraction cracks, pressure ridges, and wet cracks (Fig. 3.3). A number of small contraction cracks with lengths of a few to tens of meters appeared on the surfaces of the lakes (Fig. 3.3b). These contraction cracks penetrated the ice to depths of 10–30 cm from the surface, and did not extend to the bottom-water layer (Fig. 3.3c). These contraction cracks are considered to form by daily thermal stress within an ice sheet (Evans & Untersteiner, 1971). Contraction cracks usually form on the top surface of an ice sheet when volume contraction occurs due to cooling of the surface (Evans & Untersteiner, 1971).

On Orog Lake, we found pressure ridges with lengths of several hundred meters to a few kilometers (Fig. 3.3d–f), in which one surface ice layer largely overlies another (Fig. 3.3d). In sea ice on oceans, similar pressure ridges are known to form due to collisional compression of two floes induced by winds or currents (Arya, 1973). However, in the closed-basin lake, the pressure ridges are considered to have been formed by compressive force owing to pressure from bottom-water generated during growth of ice sheet and/or expansion of the surface ice (Dionne, 1979) for the following reasons. First, the thickness of the overlying ice layer was ~30 cm (Fig. 3.3d), indicating that the pressure ridges formed after substantial growth of the ice sheet over the lake. Second, the fact that some contraction cracks appeared to be cut by the pressure ridges (Fig. 3.3f) indicates that the lake ice grew prior to the formation of the pressure ridges. Finally, our aerial photographs show that the pressure ridges formed Y-shaped linear fractures on the lake (Fig. 3.3e), which typically form in elastic materials under compression (e.g., Yavuz et al., 2006). These features strongly suggest that the pressure ridges formed by fracturing due to compressive force. Westerly wind is unlikely to be the major source of stress for the surface ice because this cannot explain the Y-shaped linear fractures, whose direction does not match that of westerly wind.

On Orog Lake, we also found wet cracks formed by tensile forces owing to expansion of the surface ice (Fig. 3.3g). The wet cracks were typically 20–30 cm in width and ~10 m in length (Fig. 3.3g). The wet cracks were filled with whitish ice veins, which extended down to the bottom-water (Fig. 3.3g). The salinity of the whitish ice was as high as the bottom-water (Section 3.3.2), suggesting that the wet cracks were filled with upwelled bottom-water. Our aerial photographs also showed that the wet fractures were usually associated with lobate features on the ice surface (Fig. 3.3h), suggesting that they were likely formed by eruption and outflow of pressurized bottom-water after the wet

crack's formation. Although these observations suggest that the wet cracks were formed by tensile forces within the ice, several possibilities can be considered as the source of the tensile force. One is that it is due to an overshoot of the sliding surface ice sheet after the formation of pressure ridges (Parmerter & Coon, 1972). Another possibility is that it is a stress due to pressurized bottom-water after growth and volume expansion of the ice sheet. This could be supported by the fact that the bottom-lake water overflowed when our drill reached the bottom-waters.

### 3.3.2 Salinity trapped in ice

Figure 3.4 shows vertical profiles of the salinity and approximate alkalinity (see Sec. 3.2.2) in lake ice collected from Olgoy and Orog lakes in January 2020. The ice salinity was calculated by summing the concentrations (ppm = mg per kg of solution) of the major ions (i.e.,  $\text{Na}^+$ ,  $\text{K}^+$ ,  $\text{Mg}^{2+}$ ,  $\text{Ca}^{2+}$ ,  $\text{Cl}^-$ , and  $\text{SO}_4^{2-}$ ) within the collected ice samples. The results of the preliminary survey in February 2019 are also shown in Fig. A2 in Appendix A. As described in Sec. 3.2.2 above, we cannot directly obtain  $[\text{HCO}_3^-]$  and  $[\text{CO}_3^{2-}]$  in the ice samples; thus, they are not included in the ice salinity shown in Fig. 3.4. Although additions of  $[\text{HCO}_3^-]$  and  $[\text{CO}_3^{2-}]$  would increase the ice salinity, the vertical profiles of approximate alkalinity broadly follow the ice salinity profile (Fig. 3.4). Thus, the measured trend of the ice salinity would not change significantly when considering  $[\text{HCO}_3^-]$  and  $[\text{CO}_3^{2-}]$ . Figure 3.4 and Fig. A2 of Appendix A indicate that the salinity generally increases with depth. For example, the salinity increases by more than 10 times from the surface to bottom at all the sampling sites in Olgoy Lake (Fig. 3.4a). The salinity of the bottom of the lake ice typically exceeds 1000 ppm. The salinity of whitish ice veins within wet cracks (Section 3.3.1) is remarkably high (2500–4000 ppm; Fig. 3.4b). The salinity of the ice sample that contained contraction cracks is comparable to the surrounding ice (Fig. 3.4a), indicating that the contraction cracks do not extend to the bottom-water; therefore, they do not have a major role in the partitioning of salinity between the ice and bottom-water.

Figure 3.4 shows that the vertical profiles of salinity do not change significantly at the different sampling sites in Olgoy Lake (e.g., variations of 30%–40%). In contrast, for Orog Lake, there are significant spatial variations in the salinity profiles (Fig. 3.4). The ice salinity in the western part of Orog Lake is generally higher than in its central part. This reflects the relatively high salinity of the western part of the lake in warm seasons, because river water with a low salinity is supplied into its central part (Table A1 in Appendix A). In the central part of Orog Lake (i.e., sampling locations Orog\_2020C2 and Orog\_2020C3), the salinity becomes very low at depths of 30–40 cm. This may be

because the sampling sites Orog\_2020C2 and Orog\_2020C3 are close to the inlet of Tuin River (Fig. 3.2). As described in Section 3.2.1, we found that underground water inflow occurs at a low flux even in February near Tuin River. The very low salinity at the sampling sites Orog\_2020C2 and Orog\_2020C3 might have been due to the dilution of local bottom-water by this underground water.

### 3.3.3 Chemical compositions of the ice and bottom-water

Figure 3.5 shows the average chemical compositions of the ice samples compared with those of the bottom-water in cold seasons (Table A3 in Appendix A) presents the dataset of dissolved species, pH, DO, ORP, EC, and temperature of the bottom-waters) and lake water in warm seasons (Table A1 in Appendix A). Figure 3.5 shows that the major chemical components in the lake ice are  $\text{Na}^+$ ,  $\text{Cl}^-$ , and  $\text{SO}_4^{2-}$ , similar to the major dissolved ions in the lake waters in warm seasons (Table A1 in Appendix A). The relative abundances of the cations and anions in the ice are generally similar to those of the bottom-water (Fig. 3.5). The absolute abundances of the cations and anions in the ice are 20%–30% of the lake water in warm seasons and 2%–10% of the bottom-water (Fig. 3.5). The high salinity of the bottom-water was caused by the growth of lake ice (Section 3.6). Higher salinity in the lower part of the ice resulted from the entrapment of higher salinity bottom-water within the ice. A detailed evaluation of the partitioning of salinity between the ice and lake water is discussed in Section 3.6.

In the bottom-water, the concentrations of  $\text{Ca}^{2+}$  and  $\text{K}^+$  increased by only a few times over that of the lake water in warm seasons in Olgoy Lake and the central part of Orog Lake. For the other conservative cations and anions, such as  $\text{Na}^+$  and  $\text{Cl}^-$ , the concentrations increased about 10 times over that of the initial lake water (Fig. 3.5). This is because the concentration of  $\text{Ca}^{2+}$  is controlled by the solubility product of precipitated calcium carbonate (i.e., MHC) (Fukushi et al., 2020; Fukushi & Matsumiya, 2018) (Section 3.5). Precipitation of calcium carbonate prevents an increase in  $\text{Ca}^{2+}$  concentrations in the bottom-water. The  $\text{Mg}^{2+}$  concentrations and alkalinity can also be explained by Mg-carbonate precipitation (i.e., amorphous magnesium carbonate [AMC]; Section 3.5). Since the solubility product of carbonate minerals tend to be higher at lower temperatures (e.g., Marion et al., 2010), Mg concentrations both in ice samples and bottom-lake water during cold seasons are considered to become higher than that of warm season (Fig. 3.5).

The causative mechanisms for the relatively low  $\text{K}^+$  concentrations in the bottom-water of Olgoy Lake and the central part of Orog Lake are unclear. One possibility is an ionization interference from  $\text{Na}^+$  during ICP-OES analysis (e.g., Morishige &

Kimura, 2008). Another possibility is incorporation of  $K^+$  into interlayers of clay minerals in the lake deposits. However,  $K^+$ -dominant clay minerals are generated when the  $Na^+/K^+$  ratio in a solution is  $<101.1$ , based on the ion exchange coefficients (De Sanctis et al., 2020b; Fukushi et al., 2019). Given that  $Na^+/K^+ \sim 100$  in the lake waters (Fig. 3.5),  $Na^+$  would be the predominant cation in the interlayers of clay minerals in Orog and Olgoy lakes. Thus, clay minerals are unlikely to be the major sink of  $K^+$  in the lake waters.

### 3.3.4 Mineralogy of the solid residues in ice

We obtained sufficient amounts ( $>0.1$  g) of solid residues for XRD analysis after freeze-drying of ice samples from depths  $>50$  cm at the sampling locations of Olgoy\_2020C1, Olgoy\_2020C1-crack, Olgoy\_2020C2, Olgoy\_2020S1, Olgoy\_2020S2, Orog\_2020C1, Orog\_2020C5, Orog\_2020W1, and Orog\_2020W2-crack1. Figure 3.6 shows XRD patterns of the solid residues after freeze-drying of the ice samples. For samples with insufficient material for XRD analysis, XAFS spectra of the solid residues are shown in Fig. A3 in Appendix A. The XRD patterns indicate the common presence of halite ( $NaCl$ ) and thenardite ( $Na_2SO_4$ ) in the solid residues (Fig. 3.6a–d). The presence of  $NaCl$  and  $Na_2SO_4$  is consistent with the chemical composition of the lake ice (Fig. 3.5). Given that the collected bottom-water is undersaturated with these Na-bearing salts, they must have been trapped in pores within lake ice as liquid droplets, which eventually precipitated the solid residues upon freeze-drying.

In addition to Na-bearing salts, Fig. 3.6 and Fig. A3 in Appendix A reveal the presence of trace amounts of carbonate minerals, such as calcite and MHC, in the solid residues. Given that MHC is a metastable phase of calcium carbonate, it transforms into thermodynamically stable calcite over timescales of months to years at low temperature (Fukushi et al., 2020). A previous study reported that MHC occurred in lake water in Orog and Olgoy lakes in warm seasons as suspended matter (Fukushi et al., 2020). Our results suggest that MHC was trapped within the ice as suspended matter upon freezing together with the lake water (Fig. 3.6c–d). Calcite in the solid residues might have formed by conversion of MHC within the ice or after freeze-drying (Fig. 3.6b–d). Although we found MHC in the samples collected in February 2019, our results showed no clear MHC peaks in the samples collected in January 2020 (Fig. 3.6a). The weak peak of dolomite at around  $2\theta = 31^\circ$  may be found in the samples collected in January 2020 (Fig. 3.6a–b), whereas no dolomite was found in the solid residues collected in February 2019 (Fig. 3.6c–d). This discrepancy might have been caused by the transformation of MHC (and AMC) to dolomite after sampling. We performed freeze-drying and XRD analysis within 1 month of sample collection in February 2019, whereas the samples collected in January 2020

were analyzed 13 months after sampling because of a delay in sample transportation due to COVID-19. Thus, the transformation of MHC (and AMC) to calcite and dolomite would have proceeded in the samples collected in January 2020. In addition to Na-bearing salts and carbonates, quartz and plagioclase were detected in the XRD spectra. Given these minerals occur in sediments of both lakes (Fukushi et al., 2020), their presence within the solid residues also indicates the entrapment of suspended detrital minerals and/or sediment suspension in the bottom-waters (Fig. 3.6b–d).

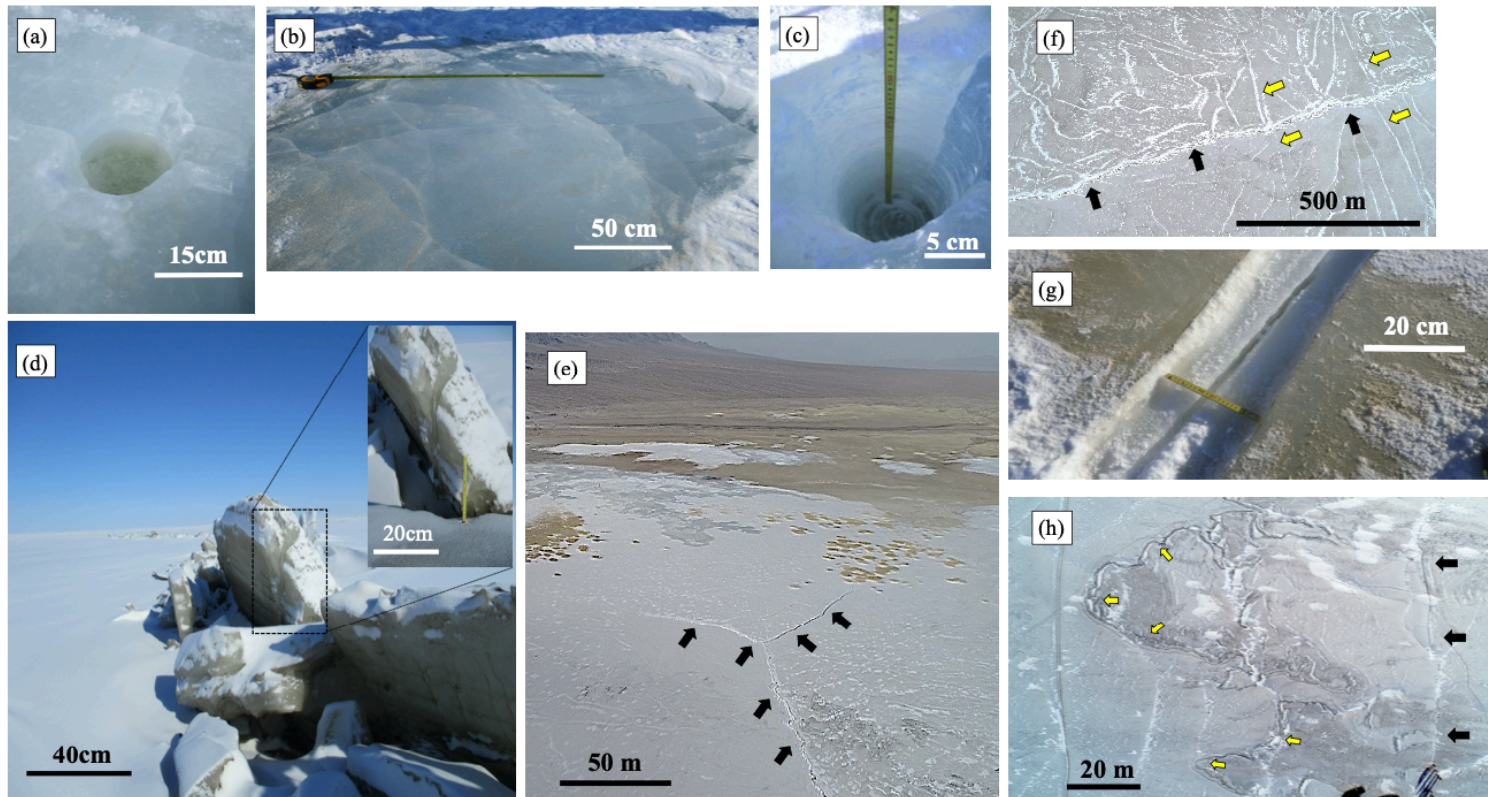


**Figure 3.3. Surface features on Orog Lake in February 2019 and January 2020.** (a) Drill hole at Orog\_2019W1 filled with bottom-water. (b) Contraction cracks. (c) Drill hole at Orog\_2019W1 across contraction cracks. (d) Pressure ridges and the overlying ice plate. (e, f) Aerial photographs of the ice surface on Orog Lake taken by a drone. Black arrows mark Y-shaped pressure ridges. Yellow arrows mark contraction cracks. (g) Wet crack at Orog\_2020W2 in the western part of Orog lake. Close-up images of whitish ice veins are shown in Fig. A1 in Appendix A. (h) Lobate features on the surface of the western part of Orog Lake. Yellow arrows mark the edges of lobate flows. Black arrows mark wet cracks.

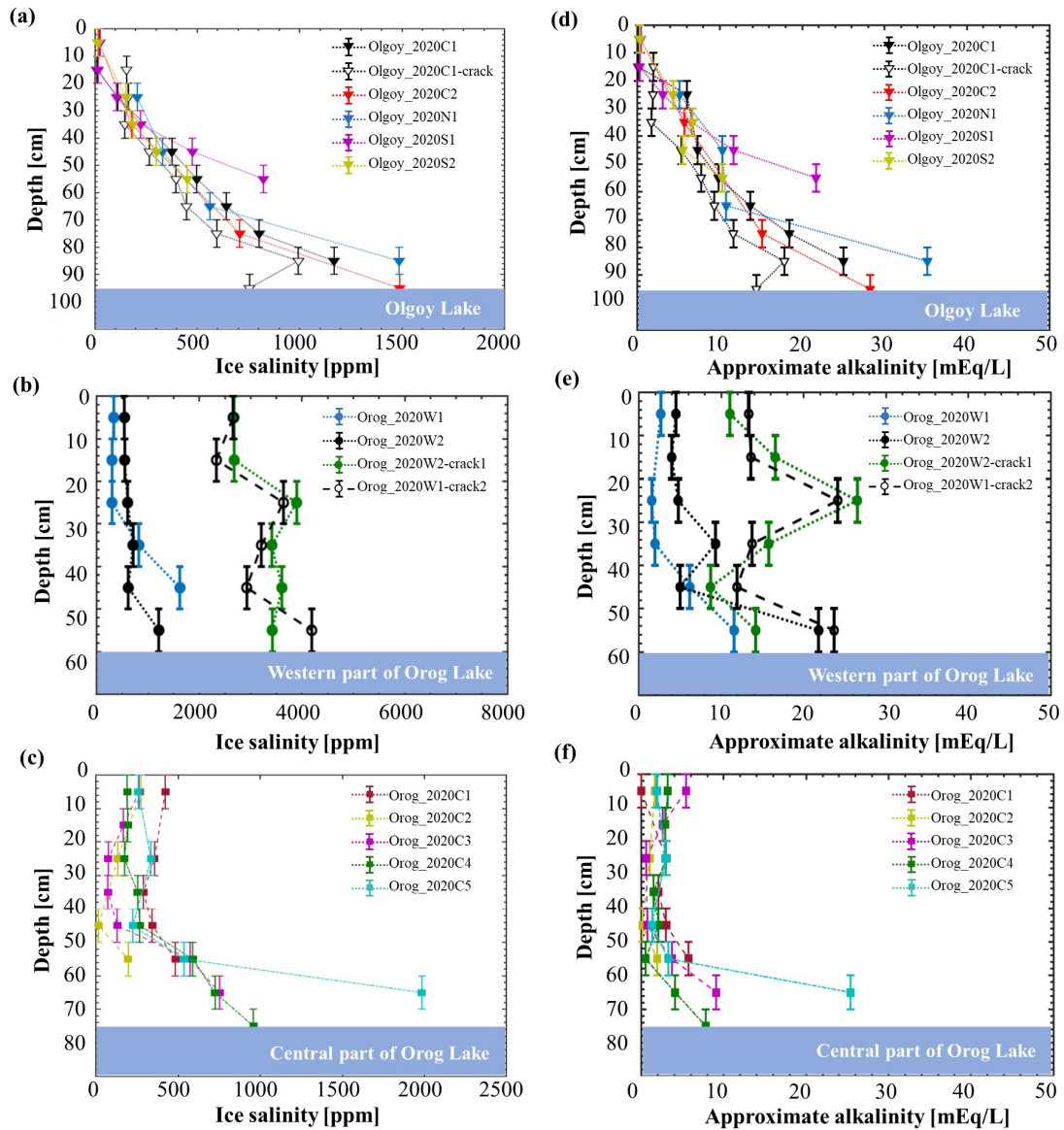


**Figure 3.4. Vertical salinity and approximate alkalinity profiles of ice samples from different sampling sites. (a, d) Olgoy Lake. (b, e) Western part of Orog Lake. (c, f) Central part of Orog Lake. The samples of Olgoy C1-crack in (a, d) include contraction cracks (Section 3.3.1). The samples of Orog W2-crack1 and W2-crack2 in (b, e) are samples from within wet cracks (Section 3.3.1). Depth errors represent the range of depth (~10 cm) over which we collected the ice samples. Table A2 in Appendix A presents the sampling locations and sample descriptions.**

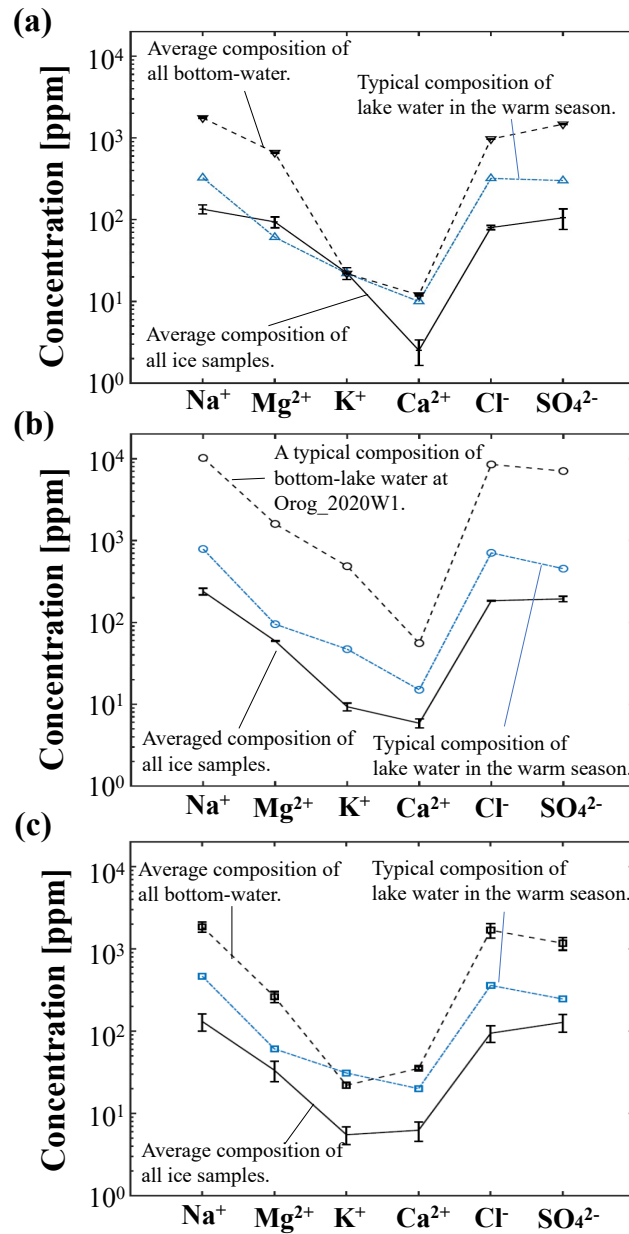


**Figure 3.5. Average compositions of major dissolved species in lake ice samples compared with those of bottom-water in cold seasons (2020) and lake water in warm seasons (2018).** (a) Olgoy Lake. (b) Western part of Orog Lake. (c) Central part of Orog Lake. Errors were calculated based on the one standard deviation of the measured values at different sampling locations in the lakes. As for the panels a) and c), we show the averaged compositions of bottom-lake water for samples collected at multiple location (see Table A2 in Appendix A); whereas, the bottom-lake water composition at location of Orog\_2020W1 is shown in the panel b) because bottom-lake water was available only at Orog\_2020W1 in the western part of Orog lake.

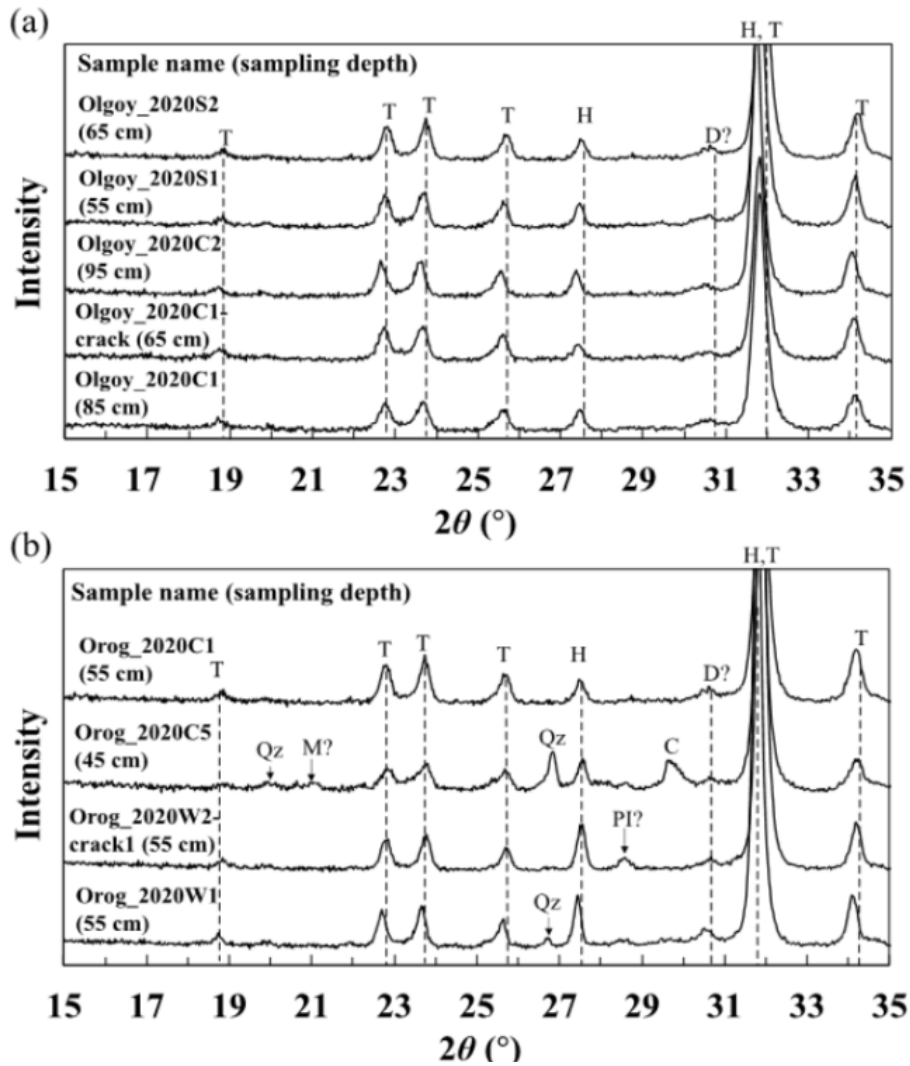


**Figure 3.6.** XRD spectra of solid residues after freeze-drying of the ice samples (H = halite; T = thernadite; M = monohydrocalcite; C = calcite; D = dolomite; Qz = quartz; Pl = plagioclase). (a) Olgoy Lake samples collected in January 2020. (b) Orog Lake samples collected in January 2020. (c) Vertical variations in XRD spectra at location Olgoy\_2019C1 (February 2019). (d) Vertical variations in XRD spectra at location Orog\_2019W1 (February 2019). The Mincrust database was used to identify halite, MHC, calcite, dolomite, quartz, and plagioclase (<http://database.iem.ac.ru/mincryst/index.php>). XRD data from the Crystallography Open Database (<https://nanocrystallography.org>) were used to identify thernadite.

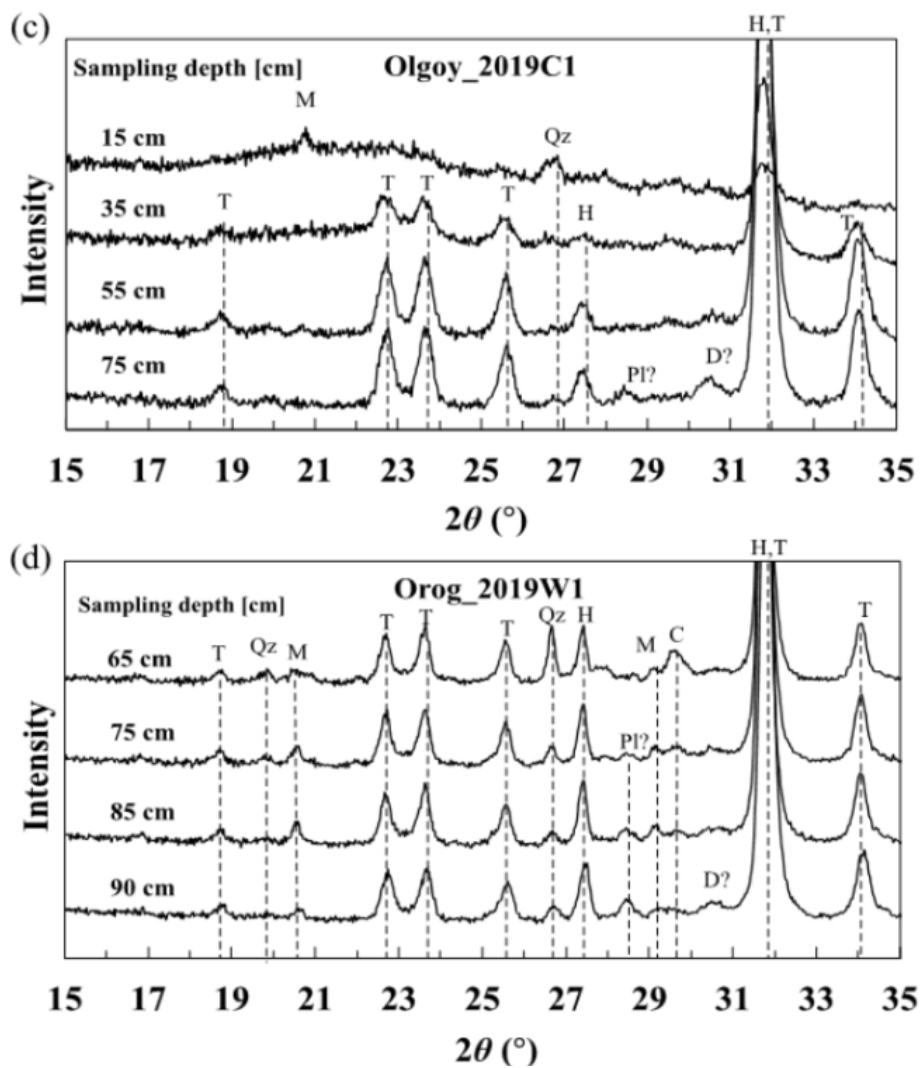


Figure 3.6. (continued).

## 3.4 Model calculations of the aqueous evolution in freezing saline lakes of Mongolia

Our data indicate that high-salinity lake water was entrapped within overlying ice upon freezing (Figs 3.4–3.5). In this section, we quantitatively interpret the results of our field investigations (Section 3.3) with a coupled mass balance and aqueous chemistry model. The aim of the calculations is to assess whether both the partitioning of salinity in the ice and chemistry of the bottom-water can be explained based on our current understanding of this system.

### 3.4.1 Model description

We considered a one-dimensional coupled mass balance and aqueous chemistry model (Fig. 3.7). This model considers stepwise growth of multiple ice layers from the lake surface to the bottom (Fig. 3.7). No interactions between the lake water and atmosphere were considered (i.e., no addition, or degassing, of CO<sub>2</sub> into, or from, the lake water), except for two calculation runs (Runs #9 and #10 in Table 3.1). In the first step of the calculations, one thin ice layer with a thickness of  $\Delta d$  (cm) was generated on the lake surface (Fig. 3.7). The thickness of a thin ice layer,  $\Delta d$ , was fixed at 5 cm in our model. A fraction of lake water entrapped in the ice layer was determined based on the theory of seawater capture for sea ice (e.g., Cox & Weeks, 1975, 1988). This model assumes entrapment of seawater in pores in between H<sub>2</sub>O ice grains of the bottom ice layer (e.g., Cox & Weeks, 1975, 1988). The entrapped total salinity,  $S_{ice}$  (ppm), in the ice layer was calculated as follows (Cox & Weeks, 1988):

$$S_{ice} = k_{eff} \times (\Sigma[X_i] + \Sigma[Y_j]), \quad (\text{Eq. 3.1})$$

where  $k_{eff}$  is the effective coefficient of lake water entrapment within ice (Section 3.4.2),  $[X_i]$  (ppm) is the concentration of dissolved species  $i$  in the lake water under the ice layer, and  $[Y_j]$  (ppm) is the concentration of precipitated solid species  $j$  in the lake water under the ice layer. Given the entrapment of suspended minerals in lake water within the ice layer (Fig. 3.6), we assumed that the precipitates were entrapped within the ice as well as dissolved species for all runs except for Run #8. In Run #8, we performed same calculations as Run #7 but assuming that precipitates were not entrapped in ice. For simplicity, no entrapment of lake water due to crack formation was considered in our model. For the ice layer in the first step, we used the lake water compositions of Oroq and Olgoi lakes in warm seasons (Table A1 in Appendix A).

In the second step of the calculations, the concentrations of dissolved species,  $[X_i]$ , and precipitated minerals,  $[Y_j]$ , in the bottom-water were calculated based on a mass

balance equation between the overlying ice layer and remaining bottom-water, as follows:

$$S_w = \frac{(L - (n - 1) \times \Delta d) \times (\Sigma[X_i] + \Sigma[Y_j]) - \Delta d \times k_{eff} \times (\Sigma[X_i] + \Sigma[Y_j])}{L - n \times \Delta d}, \quad (\text{Eq. 3.2})$$

where  $S_w$ ,  $L$ , and  $n$  are the total salinity of bottom-water, lake water depth, and number of ice layers, respectively. The total salinity  $S_w$  is the sum of  $[X_i]$  in the bottom-water.

For the remaining bottom-water, we calculated the water chemistry (pH, precipitation of minerals, and speciation of dissolved species) and freezing point depression using FREZCHEM software (Marion et al., 2010) (Section 3.4.2). We then considered the growth of an additional ice layer with a thickness of  $\Delta d$  at the bottom of the previous ice layer (Fig. 3.7). Again, the total salinity entrapped in the second layer of ice was calculated using Eq. 3.1. The calculations were continued until the ice layer reached the observed thickness of ice.

The model parameters for the calculation runs are summarized in Table 3.1. We performed calculations for seven different parameter sets (Runs #1–8 in Table 3.1). In addition to Runs #1–8, we added excess total dissolved inorganic carbon ( $\text{DIC} = [\text{CO}_2] + [\text{HCO}_3^-] + [\text{CO}_3^{2-}]$ ) to the final bottom-water for Runs #7 and #1, in order to explain the observations (we call these calculations Runs #9 and #10, respectively). Given that the salinity of lake water in the western and central parts of Orog Lake is distinct, we considered these two sub-lakes separately in our calculations. Thus, we conducted 30 calculation runs in total (Runs #1–10 for the three sub-lakes of Olgoy Lake, and the western and central parts of Orog Lake). We now describe the calculation parameters and geochemical model.

### 3.4.2 Model parameters

**Effective coefficient of entrapment of lake water in ice:** When an ice layer grows at the interface with lake or seawater, a part of the lake (or sea) water is captured within pores between the ice grains (Cox & Weeks, 1988). The effective coefficient,  $k_{eff}$ , in Eq. 3.1 is the porosity of ice formed at the interface.  $k_{eff}$  can be expressed as a function of the ice growth velocity,  $V$  (cm/s) (Cox & Weeks, 1988), as follows:

$$k_{eff} = \left[ \frac{0.26}{0.26 + 0.74 \times \exp(-7243V)} \right] \quad (V > 3.6 \times 10^{-5} \text{ cm/s}), \quad (\text{Eq. 3.3a})$$

$$k_{eff} = 0.8925 + 0.0568 \times \ln V \quad (2.0 \times 10^{-6} < V < 3.6 \times 10^{-5} \text{ cm/s}), \quad (\text{Eq. 3.3b})$$

$$k_{eff} = 0.12 \quad (V < 2.0 \times 10^{-6} \text{ cm/s}). \quad (\text{Eq. 3.3c})$$

As described in Section 3.2, the mean growth rate of the surface ice in Olgoy and Orog lakes is  $\sim 1 \times 10^{-5}$  cm/s, assuming a constant growth rate. Assuming this growth rate,  $k_{eff}$

was calculated to be 0.24 based on Eq. 3.3b. Thus, we used 0.24 for  $k_{\text{eff}}$  in our calculations. We also varied  $k_{\text{eff}}$  from a high  $k_{\text{eff}}$  (0.48) to a low  $k_{\text{eff}}$  (0.12). The low  $k_{\text{eff}}$  is the minimum value for brine capture within ice at an extremely slow growth rate, as estimated by a previous experimental study (Eq. 3.3c) (Cox & Weeks, 1988).

**Geochemical modeling of the bottom-water:** FREZCHEM can calculate the thermodynamic equilibrium compositions of minerals and dissolved species in low-temperature solutions using the Gibbs free energy minimization method (Mironenko et al., 1997; Marion et al., 2010). Table A4 in Appendix A summarizes the dissolved species and minerals considered in the present study. In addition to the original thermodynamic database, we introduced the solubility products of MHC as a function of temperature ( $\log K_{\text{sp}} = -6.99 - 200/T$ ) into FREZCHEM based on a previous experimental study (Munemoto & Fukushi, 2011). We also introduced the approximate solubility product of AMC at 5 °C ( $\log K_{\text{sp}} \sim -5.35$ ) based on a recent experimental study (Kitajima et al., 2020). The presence of AMC has not been confirmed in our samples; however, AMC needs to be present for the formation of MHC (Fukushi et al., 2017), which is found in our samples (Fig. 3.6). Although the solubility product of AMC depends on temperature, we assumed there was no temperature dependence, because of a lack of experimental data. Considering that the solubility product usually increases with a decrease in temperature, our model provides a lower limit of the  $\text{Mg}^{2+}$  concentration in bottom-water at  $-0.4$  °C. The effect of the temperature dependence is discussed in Section 3.5.

Previous studies have shown that precipitation of thermodynamically stable carbonate minerals, such as calcite and dolomite, are often suppressed in natural lacustrine environments due to the kinetics of their formation (e.g., Baker & Kastner, 1981; Fukushi & Matsumiya, 2018). Instead, metastable carbonate minerals (e.g., MHC and AMC) are precipitated, and control the water chemistry (e.g., alkalinity and pH) of lake waters in alkaline saline lakes (e.g., Fukushi et al., 2017; Fukushi & Matsumiya, 2018). To investigate the effects of metastable carbonate minerals on the chemistry of the bottom-waters, we considered three cases for precipitation of carbonates. In the first case, precipitation of dolomite was suppressed (Runs #1–5 in Table 3.1). This was conducted because precipitation of dolomite tends to be inhibited due to formation kinetics in natural environments (Fukushi et al., 2017). Due to suppression of dolomite, calcite and magnesite form as Ca- and Mg-carbonate, respectively (Section 3.4.3). In the second case, no Mg carbonate minerals were suppressed (Run #6) and thermodynamically stable dolomite and magnesite form (Section 3.4.3). In the last case, precipitation of all carbonate minerals were suppressed, except for MHC and AMC (Run #7 and Run #8).

In addition to the above calculations, we added excess DIC into the final bottom-water in Runs #7 and #1 to explain the observation (i.e., Runs #9 and #10, respectively). Through trial and error, the amount of added DIC was varied such that the results matched the observations. In Run #9, we added CO<sub>2</sub> into the bottom-water of Run #7 until the calculated pH matched the observation. In Run #10, we added CO<sub>2</sub> into the bottom-water of Run #1 to reproduce the observed Mg<sup>2+</sup> concentration, because the calculated pH for Run #10 cannot match the observation (Section 3.5). The amounts of added DIC are listed in Table 3.1.

**Lake depth:** Given that we considered a one-dimensional model, the total lake depth, *L*, approximately corresponds to the average depths of Orog and Olgoy lakes. The observed lake depths range from 60–100 cm for the western part of Orog Lake, 100–130 cm for the central part of Orog Lake, and 60–150 cm for Olgoy Lake, depending on the sampling sites (Table A2 in Appendix A). Based on the observations, we considered *L* to be a free parameter in the model by varying *L* from 95–140 cm for Olgoy Lake, 61–90 cm for the western part of Orog Lake, and 75–120 cm for the central part of Orog Lake (Table 3.1).

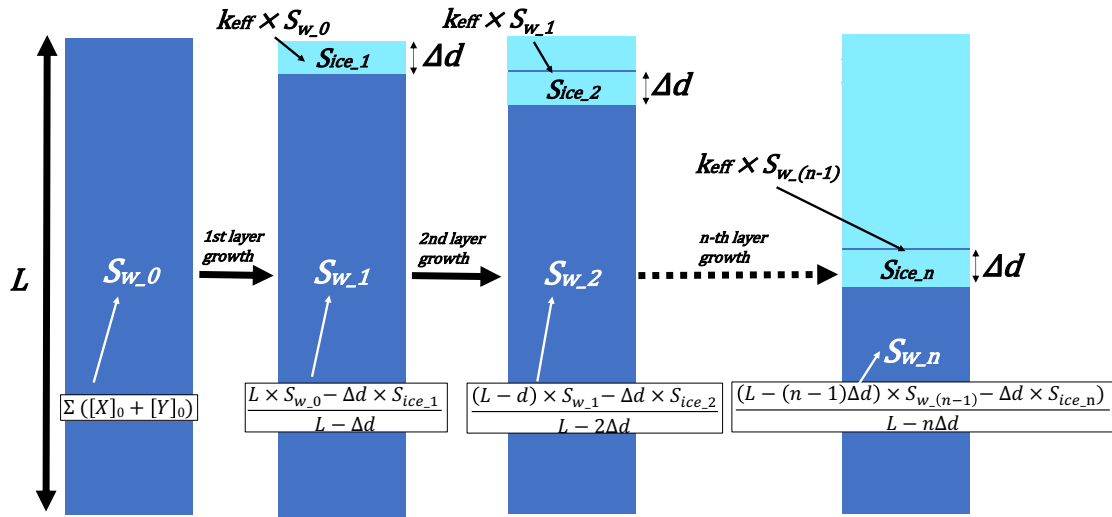


**Figure 3.7. Schematic illustration of our model for partitioning of salinity between ice and lake water upon freezing.** Blue boxes represent lake water and light blue boxes represent ice layers with a thickness of  $\Delta d$ . The parameter  $L$  is lake water depth. Freezing of lake water proceeds from left to right. In each calculation step, we obtained the salinity of a new ice layer. The mixing of remaining bottom water was assumed in each calculation step. The chemical composition of the bottom-water was then calculated. The equations shown in the figure are Eqs 3.1–3.2.

**Table 3.1. Model calculation parameters. MHC (monohydrocalcite). AMC (amorphous magnesium carbonate).**

<b>Run name</b>	<b>Run #1</b>	<b>Run #2</b>	<b>Run #3</b>	<b>Run #4</b>	<b>Run #5</b>	<b>Run #6</b>	<b>Run #7 Run #8</b>	<b>Run #9</b>	<b>Run #10</b>
<b>k<sub>eff</sub></b>	0.24	0.48	0.12	0.24	0.24	0.24	0.24	0.24	0.24
<b>Suppressed carbonate minerals</b>	Dolomite	Dolomite	Dolomite	Dolomite	Dolomite	Calcite	All carbonates except for MHC and AMC	All carbonates except for MHC and AMC	Dolomite
<b>Ice thickness [cm]</b>									
Olgoy Lake	90	90	90	90	90	90	90	90	90
Western part of Orog Lake	60	60	60	60	60	60	60	60	60
Central part of Orog Lake	70	70	70	70	70	70	70	70	70
<b>Lake depth <i>L</i> [cm]</b>									
Olgoy Lake	100	100	100	95	140	100	100	100	100
Western part of Orog Lake	65	65	65	61	80	65	65	65	65
Central part of Orog Lake	85	85	85	75	120	85	85	85	85
<b>Amounts of added DIC [mmol/L]</b>									
Olgoy Lake	-	-	-	-	-	-	-	8.5	22
Western part of Orog Lake	-	-	-	-	-	-	-	32	85
Central part of Orog Lake	-	-	-	-	-	-	-	9.6	21

### 3.4.3 Model results

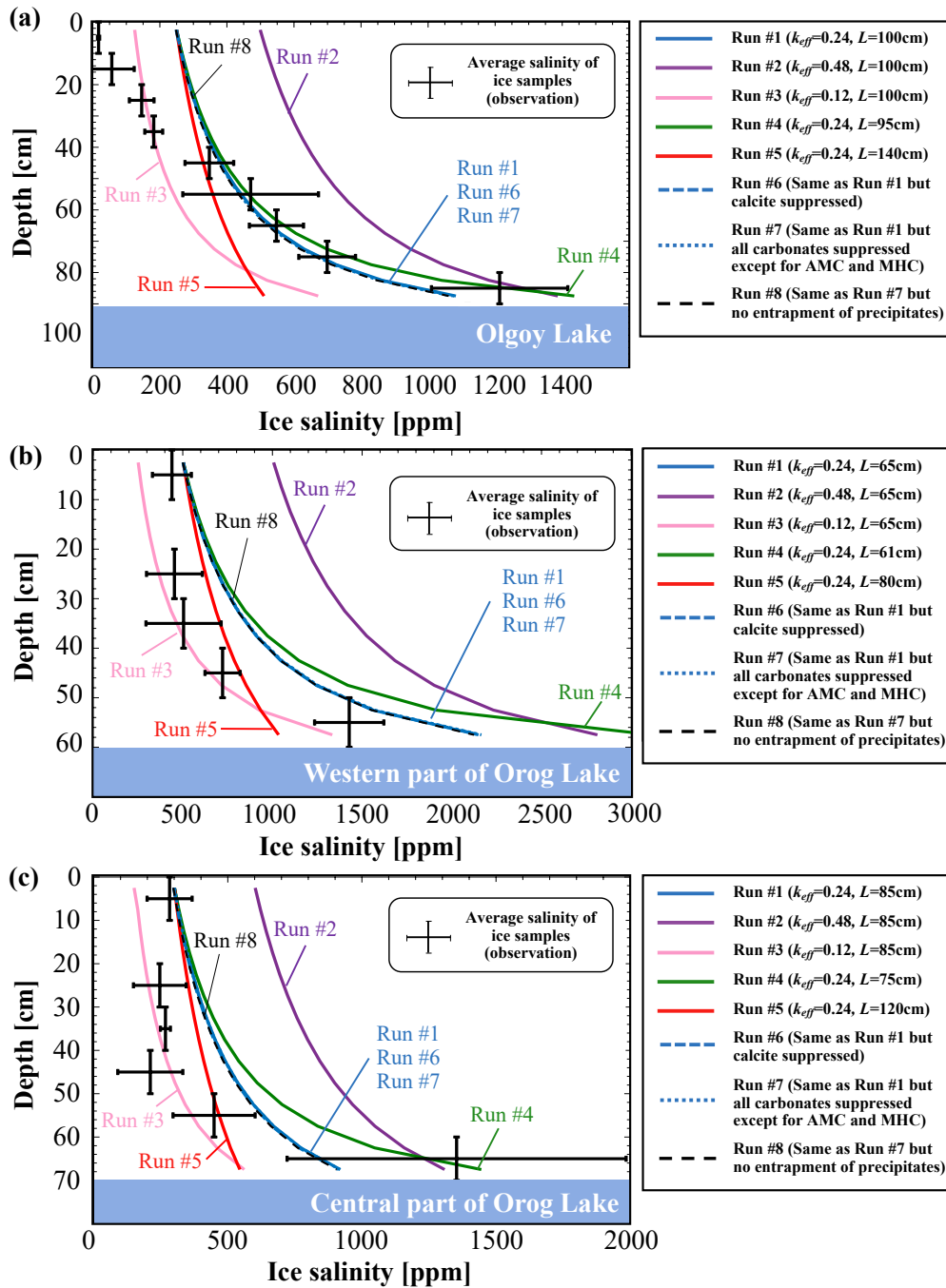
Figure 3.8 shows the model results for the salinity in lake ice as a function of lake depth for different model parameters for Orog and Olgoy lakes compared with the observations at different sampling sites. As well as the ice salinity in the field survey (Section 3.4.2), the salinity in lake ice was obtained in the model calculations by summing concentrations of  $\text{Na}^+$ ,  $\text{K}^+$ ,  $\text{Mg}^{2+}$ ,  $\text{Ca}^{2+}$ ,  $\text{Cl}^-$ , and  $\text{SO}_4^{2-}$  within ice. This means that we excluded  $\text{HCO}_3^-$  and  $\text{CO}_3^{2-}$  from the modeled ice salinity as well as the measured ice salinity. A comparison of the results for Runs #1–3 (Table 3.1) in Fig. 3.8 indicates that the salinity in lake ice is proportional to  $k_{\text{eff}}$ . Comparing the effects of lake depth (Runs #1, #4, and #5), the salinity in the lower part of the ice layer becomes higher for shallower lake depths (Fig. 3.8). This is because the amount of bottom-water becomes less for shallower lakes when the same thickness of ice grows in shallower and deeper lakes. Our results also show that the salinity in lake ice depends little on the choice of suppressed carbonates (Runs #1, #6, and #7 in Fig. 3.8). This is because the contributions of precipitated carbonates to salinity in lake ice are very small compared with  $\text{Na}^+$ ,  $\text{Cl}^-$ , and  $\text{SO}_4^-$  in lake water entrapped in lake ice pores. Comparison of Run #7 and #8 in Fig. 3.8 also shows that the ice salinity changes only  $\sim 2\%$  in spite of no entrapment of precipitates. This is because the  $\Sigma[X_i]/\Sigma[Y_j]$  ratio of Eq. 3.1 is about  $\sim 50/1$ , indicating that the efficiency of entrapment of precipitates would not affect our conclusion significantly. This is consistent with the fact that halite and thenardite are predominant in the solid residues of the ice samples after freeze drying (Fig. 3.6).

Our results can reproduce the general increase in salinity of lake ice as a function of depth (Fig. 3.8), although there are a few discrepancies between the model results and observations. For example, in Olgoy Lake, the model results cannot reproduce the extremely low salinity in the upper part of the ice (Fig. 3.8a). In addition, the calculated salinity of ice for the central part of Orog Lake tends to be lower than the observations in the middle depths (Fig. 3.8b–c). The causative mechanisms of the discrepancies are discussed in Section 3.6.

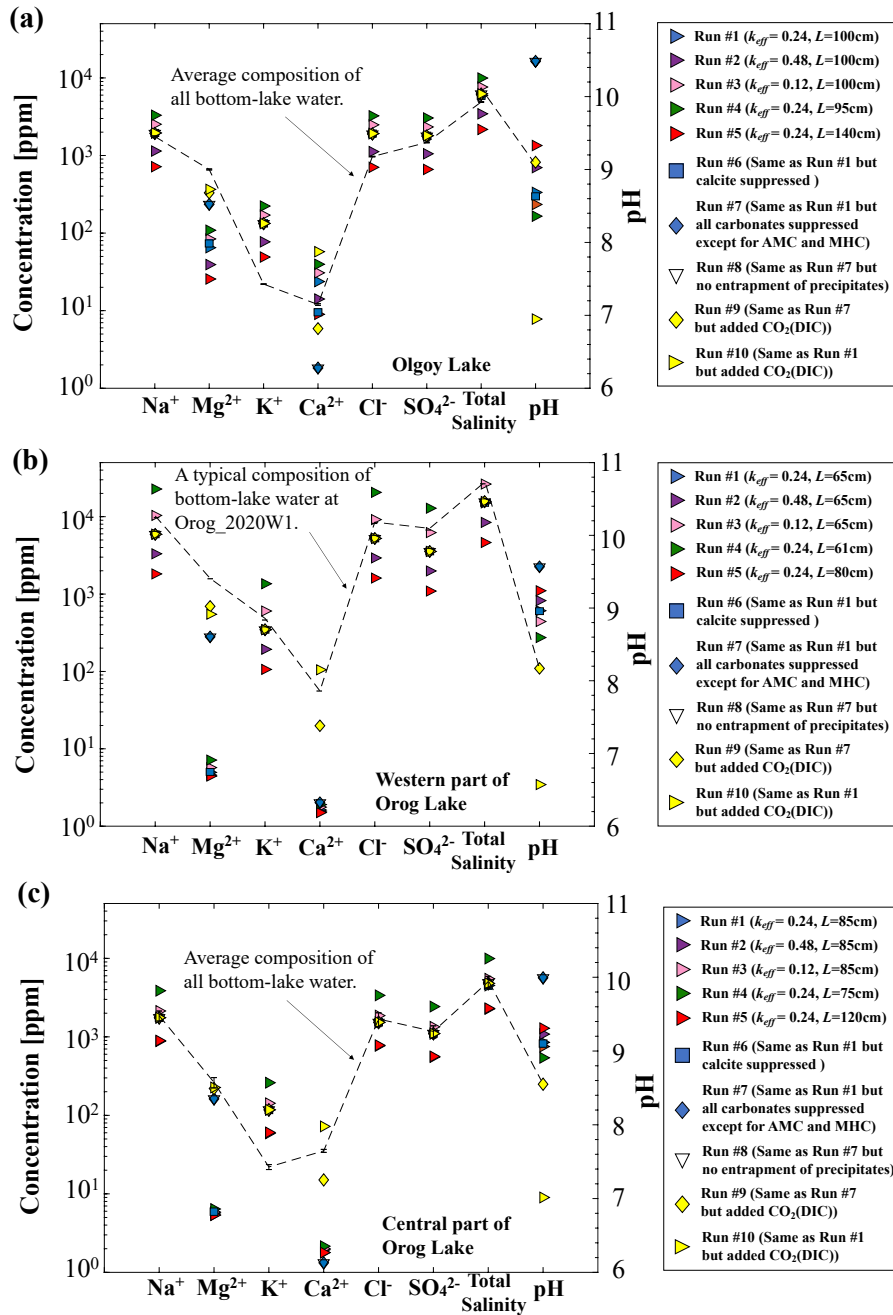
Figure 3.9 shows our model results of the concentrations of dissolved species, pH, and salinity of the bottom-water compared with the observations. The total salinity of the bottom-water is inversely proportional to  $k_{\text{eff}}$  (Runs #1–3 in Fig. 3.9). A comparison of Runs #1, #4, and #5 in Fig. 3.9 shows that the total salinity of bottom-water increases for a shallower lake depth.

Figure 3.9 also shows that the calculated concentrations of  $\text{Mg}^{2+}$  and  $\text{Ca}^{2+}$  in the bottom-water are strongly dependent on the assumptions regarding the suppression of carbonate minerals. This is because the  $\text{Mg}^{2+}$  and  $\text{Ca}^{2+}$  concentrations are controlled by the solubility products of carbonate minerals. In Run #6 with no suppression of Mg carbonate minerals (Case 2 in Table 3.1), precipitation of magnesite and dolomite can control the concentrations of  $\text{Mg}^{2+}$  and  $\text{Ca}^{2+}$  in the bottom-water during freezing, respectively (Fig. A4 in Appendix A). However, in Runs #1–5 with suppression of dolomite,  $\text{Mg}^{2+}$  and  $\text{Ca}^{2+}$  concentrations are controlled by magnesite and calcite, respectively (Fig. A4 in Appendix A). In Run #7,  $\text{Mg}^{2+}$  and  $\text{Ca}^{2+}$  concentrations are controlled by precipitation of MHC and AMC, respectively (Fig. A4 in Appendix A).

Our results show that the measured concentrations of  $\text{Mg}^{2+}$  and  $\text{Ca}^{2+}$  in bottom-water are poorly explained by our model results from Runs #1–7 (Fig. 3.9). Addition of DIC to the final bottom-water of Run #7 improves the comparison with the measured  $\text{Mg}^{2+}$  and  $\text{Ca}^{2+}$  concentrations and pH (Run #9; Fig. 3.9). Although addition of DIC to the final bottom-water of Run #1 can improve the comparison of the  $\text{Mg}^{2+}$  concentrations with the observations, the calculated  $\text{Ca}^{2+}$  concentration and pH do not match the observations (Fig. 3.9). The discrepancy between our model calculations and the observations, and the possible source of DIC to the bottom-waters are discussed in Section 3.5.



**Figure 3.8. Model results (Runs #1–8) for the ice salinity in (a) Olgoy Lake, (b) western part of Orog Lake, and (c) central part of Orog Lake compared with the field observations.** The measured ice salinity is the average value of different sampling sites with errors shown as one standard deviation. We excluded the sampling site Orog\_2020C3 because it was affected by input from underground water near the inlet rivers (Section. 3.2).



**Figure 3.9. Model results (triangles, squares, and diamonds) for bottom-water compositions (Runs #1–10). (a) Olgyo Lake. (b) Western and (c) central parts of Orog Lake.** Errors on the measured concentrations of dissolved species were calculated as the one standard deviation of the measured values at different sampling locations in the lakes. As for the panels a) and c), we show the averaged compositions of bottom-lake water for samples collected at multiple location (see Table A2 in Appendix A); whereas, the bottom-lake water composition at location of Orog\_2020W1 is shown in the panel b) because bottom-lake water was available only at Orog\_2020W1 in the western part of Orog lake. Measured pH values of Olgyo Lake, and the western and central part of Orog Lake were obtained from Olgyo\_2020C1, Orog\_2020W1, and Orog\_2020C1, respectively (Table A3 in Appendix A).

## 3.5 Interpretations of chemical partitioning based on model calculations and field observations

### 3.5.1 Olgoy Lake

Figure 3.8a shows that the calculated salinity of the upper part of lake ice (depth < 40 cm) is significantly higher than the observations. The measured salinity of the upper part of the lake ice is one or two orders of magnitude lower than the calculated salinity (Fig. 3.8a). To achieve the measured very low ice salinity,  $k_{\text{eff}}$  in the upper part of the ice must be extremely low compared with the  $k_{\text{eff}}$  of terrestrial sea ice and previous experiments (e.g., Weeks & Lofgren, 1967). The extremely low  $k_{\text{eff}}$  could be achieved if the freezing rate of ice was  $\ll 10^{-6}$  cm/s (Eq. 3.2c). However, this is highly unlikely given that formation of lake ice with a thickness of  $\sim 1$  m occurs within several months on Olgoy Lake (Section 3.3). Additions of  $\text{H}_2\text{O}$  via rain and snow are negligible in cold seasons (Section 2).

One explanation for the extremely low salinity in the upper part of the lake ice in Olgoy Lake is that the entrapped water had a very low salinity when ice in the upper part formed. The major water source for Olgoy Lake is groundwater seepage that has a very low salinity (Sekine et al., 2020). If groundwater seepage continued after the formation of the thin ice layer (e.g., ice thickness < 30 cm) in Olgoy Lake, the low-salinity groundwater could have been supplied to near the boundary between the ice and bottom-water due to the low density of low-salinity groundwater. After the formation of ice with a thickness of  $\sim 40$  cm, groundwater seepage might have ceased due to further decreases in air temperature. Given the diffusion coefficient of  $\text{Na}^+$  and  $\text{Cl}^-$  in water ( $\sim 10^{-9}$  m/sec: e.g., Vitagliano & Lyons, 1956), the salinity stratification with thickness of  $\sim 40$  cm could be maintained for several months.

Alternatively, the extremely lower  $k_{\text{eff}}$  might have been caused by differences in the mode of ice crystal growth at the interface. Previous studies have reported that a transition from a planar liquid–solid interface to a cellular interface between ice and seawater occurs because of an increase in water salinity (Lofgren & Weeks, 1969; Weeks & Lofgren, 1967). The present study implicitly assumed a cellular interface between ice and lake water. The  $k_{\text{eff}}$  of a cellular interface reflects the ice porosity, which is controlled by the freezing rate as shown in Eq. 3.3 (Cox & Weeks, 1975, 1986). A cellular interface tends to occur when the water salinity is high (e.g., Gross et al., 1977). In contrast, a planar interface tends to occur during freezing of low-salinity water (Gross et al., 1977). The  $k_{\text{eff}}$  of a planar interface is known to be several orders of magnitude lower than that of a cellular interface (e.g., Weeks & Lofgren, 1967). The extremely low  $k_{\text{eff}}$  in the upper part of lake ice in Olgoy Lake can be explained by the occurrence of a planar interface due to the low-salinity lake water. Upon freezing of the

lake water, the salinity of the bottom-water would have increased, and a transition to a cellular interface might have occurred after the growth of ice to a thickness of ~40 cm. Ice formed with planar interface would exhibit an aligned ice grain boundary (e.g., Weeks and Lofgren, 1967). This could be confirmed with microscopic observations of ice samples in future work.

Apart from the upper part of the ice, the ice salinity is well explained by our model calculations, especially for ice thickness of 50 and 90 cm (Runs #1, #4, #6, and #7) (Fig. 3.8a). In Runs #1, #6, and #7, the calculated total salinity of the bottom-water is about 6000 ppm, which agrees with the measured value (Fig. 3.9a). These results suggest that the  $k_{\text{eff}}$  would have been close to the standard value (~0.24), which was obtained from the average freezing rate of ice in Olgoi Lake (Eq. 3.3b). Figure 3.9a shows that the concentrations of  $\text{Na}^+$ ,  $\text{Cl}^-$ , and  $\text{SO}_4^{2-}$  of Runs #1, #4, #6, and #7 are generally consistent with the measured values (i.e., within a factor of 2).

As described in Section 3.4.2, there is a major discrepancy between the calculations and observations for the  $\text{Mg}^{2+}$  concentrations and pH values of the bottom-water (Fig. 3.9). In Runs #1–6, the measured  $\text{Mg}^{2+}$  concentrations in the bottom-water are poorly explained by the model (Fig. 3.9a). Compared with Runs #1–6, the calculated  $\text{Mg}^{2+}$  concentration in Run #7 is higher due to the high solubility product of AMC. However, the calculated  $\text{Mg}^{2+}$  concentrations are still ~50% of the measured values (Fig. 3.9a). In addition, the calculated pH of Run #7 is too large to explain the measured pH (Fig. 3.9). Thus, the results of Runs #1–7 cannot explain both the  $\text{Mg}^{2+}$  concentrations and pH values of the observations.

One possible explanation for the underestimation of  $\text{Mg}^{2+}$  concentrations is that our calculations provide lower limits of  $\text{Mg}^{2+}$  concentrations, because we used a constant solubility product for AMC at 5 °C (Kitajima et al., 2020). Given that the solubility product of AMC tends to increase at lower temperatures (Kitajima et al., 2020) (Section 3.4.2),  $\text{Mg}^{2+}$  concentrations at -0.4 °C (i.e., the temperature of the bottom-water; Table A3 in Appendix A) would be higher than our model results. The solubility product of AMC was estimated to be  $10^{-5.35}$  at 5 °C (Kitajima et al., 2020) and  $10^{-5.6}$  at 25 °C (Fukushi & Matsumiya, 2018). By extrapolating the previous results assuming the temperature dependence of  $1/T$ , the solubility product of AMC could be  $\sim 10^{-5.27}$  at -0.4 °C. If this is the case, an increase in the solubility product at -0.4 °C could explain the discrepancy in Mg concentration between the observation and calculation in a factor of 2–3. Further investigations on temperature dependency of the solubility product of AMC would be required to more constrain the water chemistry of freezing Orog and Olgoi lakes.

An alternative explanation is that our model underestimates DIC in the bottom-water. In fact, the calculated DIC in the bottom-water is about 5% of the DIC estimated

from the measured alkalinity (Table A3 in Appendix A). This implies that an additional source of DIC to the bottom-water is required to explain the measured high DIC in the bottom-water. Figure 3.9a shows that the results of Run #9 with addition of DIC to the final bottom-water of Run #7 greatly improves the comparison between the calculations and observations by a factor of 2–3.

However, addition of DIC into the final bottom-water of Run #1 cannot reproduce the measured pH value (Run #10 in Fig. 3.9a). To explain the high Mg concentration, the DIC needs to be increased. However, given that the calculated pH of Run #1 is already lower than the observed pH, addition of DIC results in further lowering of the pH. After adding DIC until the calculated  $\text{Mg}^{2+}$  concentrations become close to the observations, magnesite and calcite are completely dissolved into the lake water of Run #10, which is also inconsistent with the observations. These results suggest that metastable phases of carbonate (i.e., AMC and MHC) are important to explain the observations, along with addition of DIC.

The source of DIC to the bottom-water is unclear. Addition of DIC could have occurred through interactions with the atmosphere when pressurized cracks and wet cracks formed on the lakes. In addition, decay of organic matter on the lake floor by dissolved  $\text{O}_2$  could provide additional DIC, given the concentrated DO levels of the bottom-water ( $\text{DO} = 13\text{--}18$  mg/L; Table A3 in Appendix A). In the case of Olgoy lake, the excess DIC in Run #9 required to explain the observations is about  $\sim 8.5$  mmol/L. On the other hand, an increase in DIC in the bottom-lake water due to re-equilibrium with the atmospheric  $\text{CO}_2$  (400 ppm) is calculated to be  $\sim 6.1$  mmol/L. Thus, exchange with atmospheric  $\text{CO}_2$  may be insufficient to explain the required excess DIC, calling for an additional source of DIC, such as decay of organic matter. Same as Olgoy lake, the excess DIC required to explain the observation of Orog lake (32 and 9.6 mmol/L for the western and central parts of Orog lake, respectively) could not be achieved solely by exchange with the atmosphere (18 and 7.2 mmol/L for the western and central parts of Orog lake, respectively).

Figure 3.9a shows that the calculated concentrations of  $\text{K}^+$  are significantly higher than the measured values. As discussed in Section 3.3.3, the discrepancy between the model results and observations may be partly due to an ionization interference from  $\text{Na}^+$ . Alternatively, an unknown process that can effectively trap  $\text{K}^+$  in the sediments (e.g., formation of illite: see Fukushi et al. (2020) for mineralogy of lake sediments) could reduce the observed  $\text{K}^+$  concentrations in the bottom-waters.

### 3.6.2 Orog Lake

Figure 3.8b shows that the calculated salinity of the upper part of lake ice agrees with the observations in the western part of Orog Lake. This indicates there was no significant input of low-salinity water into the western part of Orog Lake, as the major water source for Orog Lake is Tuin River that flows into the central and eastern parts of the lake (Section 3.2). The water of Orog Lake in warm seasons contains high concentrations of authigenic carbonate minerals (e.g., MHC) as suspended materials (Fukushi et al., 2020). Any impurities, such as suspended materials, would affect the morphology of ice crystal growth (Nagashima & Furukawa, 2000), possibly leading to effective formation of a cellular interface and high  $k_{\text{eff}}$ .

Figure 3.8b suggests that the average  $k_{\text{eff}}$  for the western part of Orog Lake varied from 0.12–0.24, which is consistent with, or slightly lower than, the average freezing rate of the lake. The calculated ice salinity in the bottom part of the ice becomes lower than the measured salinity (Fig. 3.8b), although the calculated salinity of Run #4 (i.e., a shallow lake depth) falls within the range of the measured values. The calculated salinity in the bottom-water in the case of a shallow lake depth (Run #4) is also consistent with the observations (Fig. 3.9b). These results indicate that the observations can be explained by our model if the freezing rate is slow (i.e., a low  $k_{\text{eff}}$ ) in the upper part of the ice, and if the freezing rate is increased in the lower part of the ice possibly due to low air temperatures in January and February. Although more precise fitting of the observed data can be achieved by changing  $k_{\text{eff}}$ , this is beyond the scope of the present study. Our results suggest that the ice salinity could be affected by variations in freezing rate over time.

Like Olgoy Lake, there is a discrepancy in  $\text{Mg}^{2+}$  and  $\text{Ca}^{2+}$  concentrations and pH values between our calculations and observations (Fig. 3.9b). We again suggest that our model would underestimate DIC in the bottom-waters. In fact, the calculated DIC in the bottom-water is about 20% of the measured DIC estimated from the alkalinity (Table A3 in Appendix A), suggesting addition of DIC into the bottom-water. Our results show that addition of DIC into the bottom-water in Run #9 improves the comparison between  $\text{Mg}^{2+}$  and  $\text{Ca}^{2+}$  concentrations and pH values between the model calculations and observations by a factor of 2–3 (Fig. 3.9b). A comparison of Runs #9 and #10 highlights the importance of MHC and AMC in explaining the measured pH values (Fig. 3.9b).

For the central part of Orog Lake, the calculated ice salinity for low  $k_{\text{eff}}$  tends to match the observations in the upper part of the ice, similar to the western part of Orog Lake (Fig. 3.8c). Our results also show that the calculated ice salinity for high  $k_{\text{eff}}$  is consistent with the observations in the bottom part of the ice (Fig. 3.8c). This suggests that the freezing rate would have changed significantly during freezing of the lake.

Similar to Olgoy Lake and the western part of Orog Lake, our results show that addition of DIC greatly improves the agreement with the measured  $\text{Mg}^{2+}$  and  $\text{Ca}^{2+}$  concentrations and pH values (Fig. 3.9c). The discrepancy in the  $\text{K}^+$  concentration between the model calculations and observations could also be due to an ionization interference from  $\text{Na}^+$  or unknown processes that can trap  $\text{K}^+$  in sediments (e.g., formation of illite: see Fukushi et al. (2020) for mineralogy of lake sediments).

### 3.6 Implications for subsurface brine reservoir on icy bodies

The key findings of our field observations are:

- (1) We found three types of cracks and ridges on the Orog and Olgoy lakes: contraction cracks, pressure ridges, and wet cracks. Pressure ridges were formed by compressive forces due to volume expansion of ice, whereas wet cracks were likely formed by tensile forces. The deformation of ice plate after the formation of pressure ridge would likely form wet cracks, filled with ice that had a similar composition as the bottom-water.
- (2) In general, the salinity of the lake ice increased as a function of ice depth. This is due to entrapment of highly saline bottom-water within pores of ice upon freezing. The ice salinity was locally influenced by dilution due to seepage of groundwater into the freezing lakes.

Point (1) suggests that even in a simple monotonically freezing liquid reservoir, different types of force (i.e., compressive and tensile) can occur in the overlying ice. Freezing leads to changing volumes of  $\text{H}_2\text{O}$ , which, in turn, would cause deformations and fracturing. Some cracks (e.g., wet cracks) could allow delivery of subsurface brine to the surface. This complex behavior could happen in lenticulae features and ridges on Europa, if the thickness of ice overlying a subsurface brine reservoir is sufficiently thin to avoid the occurrence of solid-state convection of the ice. If a subsurface brine reservoir is shallow (e.g.,  $< 10$  km in depth), the complex behavior of ice tectonics could transport salinity from the subsurface brine reservoir to the surface.

The comparison of our model calculations with the field observations suggests that:

- (1) A change in freezing rate affects the salinity of lake ice when a cellular interface develops at liquid–solid interface. A change in the freezing rate may affect the ice salinity by a factor of 2–3.

- (2) In order to explain the  $\text{Mg}^{2+}$  and  $\text{Ca}^{2+}$  concentrations in the bottom-waters, metastable phase of carbonate (i.e., AMC and MHC) are required. As such, formation of more stable dolomite, calcite, and magnesite would be suppressed or have little role in controlling the  $\text{Mg}^{2+}$  and  $\text{Ca}^{2+}$  concentrations in the freezing lakes. Furthermore, addition of DIC into the bottom-water is required to explain the  $\text{Mg}^{2+}$  and  $\text{Ca}^{2+}$  concentrations and pH values of the bottom-waters.
- (3) Our simple model can reproduce the general salinity trends, particularly for conservative dissolved species, such as  $\text{Na}^+$ ,  $\text{Cl}^-$ , and  $\text{SO}_4^{2-}$ , in the ice and bottom-waters.

Regarding point (2), the importance of metastable phases of carbonate minerals has not been previously invoked to explain the aqueous chemistry of subsurface brine reservoirs on Ceres and Europa, although one previous study suggested it might have been important for the subsurface ocean of Enceladus (Fukushi et al., 2020). If the metastable carbonate minerals control the pH and alkalinity of subsurface brine reservoirs upon freezing, DIC and divalent cation ( $\text{Mg}^{2+}$  and  $\text{Ca}^{2+}$ ) concentrations in a freezing reservoir would be significantly higher than when only stable carbonates, such as magnesite and dolomite, are considered (e.g., Castillo-Rogez et al., 2018). If this were the case, relatively high DIC contents in a subsurface brine reservoir could lead to formation of abundant carbonate in the bright spots of Ceres.

The metastable phase of carbonate (i.e., AMC and MHC) have not been identified in surface materials in previous remote-sensing studies (e.g., De Sanctis et al., 2016), although the presence of hydrohalite ( $\text{NaCl}\cdot 2\text{H}_2\text{O}$ ) and its dehydration product ( $\text{NaCl}$ ) have been suggested to be present near the bright spots of Occator Crater of Ceres (De Sanctis et al., 2020a). Similar to hydrated  $\text{NaCl}$  (e.g., Thomas et al., 2017; Vu et al., 2016), reflectance spectra of MHC and AMC (Coleyshaw et al., 2003; Tanaka et al., 2019) could be useful in interpretation of observations of fresh surface materials. Given that the metastable carbonates transform into thermodynamically stable carbonates of calcite, magnesite, and dolomite in a certain amount of time after entrapment within ice, the presence of these metastable phases could be used to estimate the timing of eruption.

### 3.7 Summary of Chapter 3

We conducted winter field surveys of freezing hyposaline lakes (i.e., Olgoi and Orog lakes) in the Valley of Gobi Lakes, Mongolia, as terrestrial analogs of freezing subsurface brine reservoirs on icy bodies in the Solar System. We observed the surface geomorphology of the frozen lakes and collected ice and bottom-water samples at multiple locations. Using our coupled mass balance and low-temperature aqueous chemistry model, the observational data were interpreted. We reached the following conclusions.

- The ice-covered surface was widely disrupted by cracks and ridges. Pressurized ridges were formed by compressive forces, whereas wet cracks were formed by tensile forces. Even in a simple downward freezing closed-basin lake, compressive and tensile forces can be generated due to complex tectonics. This suggests that on lenticulae features and ridges on icy bodies, there could be both extensional and compressive cracks. If tensile force forms wet cracks, they would transport salinity to the surface ice.
- The salinity of lake ice generally increased as a function of depth due to the concentration of solutes in the bottom-water. The salinity of the bottom-water increased several times over that of the lake water in warm seasons. Variable ice salinity can be caused by local inputs of groundwater seepage and changes in the ice freezing rate. Our model calculations can reproduce the general increases in ice and bottom-water salinity.
- We suggest that the metastable phases MHC and AMC are present in the freezing lakes. The  $Mg^{2+}$  and  $Ca^{2+}$  concentrations of the bottom-water can be better explained when MHC and AMC are considered. In addition to the metastable phases, DIC is also needed to explain the observations. If MHC and AMC control DIC and divalent cation ( $Mg^{2+}$  and  $Ca^{2+}$ ) concentrations in subsurface brine reservoirs of icy bodies, then DIC contents could be higher than estimates based only on thermodynamically stable carbonates. The presence of metastable carbonates on the surfaces of icy bodies could be a potential indicator of eruption of fresh materials from subsurface brine reservoirs.

## **Chapter 4. Chemical evolution of subsurface brines and formation of bright materials on Ceres**

本章については、五年以内に雑誌等で刊行予定のため、非公開。

## **Chapter 5. General Conclusions**

本章については、五年以内に雑誌等で刊行予定のため、非公開。

## References

- Alibert, T. & Mousis, O. (2006). Formation of Titan in Saturn's subnebula: constraints from Huygens probe measurements. *Astronomy & Astrophysics*, 465, 1051–1060. doi: 10.1051/0004-6361:20066402
- Arya, S. P. S. (1973). Contribution of form drag on pressure ridges to the air stress on Arctic ice. *Journal of Geophysical Research: Oceans and Atmospheres*, 78(30), 7092–7099. doi:10.1029/JC078i030p07092
- Bethke, C. (2007). *Geochemical and Biogeochemical Reaction Modeling* (2nd ed.). Cambridge: Cambridge University Press. doi:10.1017/CBO9780511619670
- Baker, P. A., & Kastner, M. (1981). Constraints on the Formation of Sedimentary Dolomite. *Science*, 213(4504), 214-216. doi: 10.1126/science.213.4504.214
- Bargery, A. S., Lane, S. J., Barrett, A., Wilson, L., & Gilbert, J. S. (2010). The initial responses of hot liquid water released under low atmospheric pressures: Experimental insights. *Icarus*, 210, 488–506. doi: 10.1016/j.icarus.2010.06.019
- Bowling, T. J., Ciesla, F. J., Davison, T. M., Scully, J. E. C., Castillo-Rogez, J. C., Marchi, S., & Johnson, B. C. (2019). Post-impact thermal structure and cooling timescales of Occator crater on asteroid 1 Ceres. *Icarus*, 320, 110-118. doi: 10.1016/j.icarus.2018.08.028.
- Buffo, J. J., Schmidt, B. E., Huber, C., & Walker, C. C. (2020). Entrainment and dynamics of ocean derived impurities within Europa's ice shell. *Journal of Geophysical Research: Planets*, 125(10), e2020JE006394. <https://doi.org/10.1029/2020JE006394>
- Carrozzo, F. G., De Sanctis, M. C., Raponi, A., Ammannito, E., Castillo-Rogez, J., Ehlmann, B. L., Marchi, S., Stein, N., Ciarniello, M., Tosi, F., Capaccioni, F., Capria, M. T., Fonte, S., Formisano, M., Frigeri, A., Giardino, M., Longobardo, A., Magni, G., Palomba, E., Zambon, F., Raymond, C. A., & Russell, C. T. (2018). Nature, formation, and distribution of carbonates on Ceres. *Science Advance*, 4, e1701645. doi: 10.1126/sciadv.1701645
- Castillo-Rogez, J. C., Hesse, M., Formisano, M., Sizemore, H., Bland, M., Ermakov, A., & Fu, R. (2019). Conditions for the long-term preservation of a deep brine reservoir in Ceres. *Geophysical Research Letters*, 46, 1963-1972. doi: 10.1029/2018GL081473
- Castillo-Rogez, J. C., & McCord, T. B. (2010). Ceres' evolution and present state constrained by shape data. *Icarus*, 205(2), 443-459. doi: 10.1016/j.icarus.2009.04.008
- Castillo-Rogez, J. C., Neveu, M., McSween, H. Y., Fu, R., Toplis, M., & Prettyman, T. (2018). Insights into Ceres' evolution from surface composition. *Meteoritics and Planetary Science*, 53(9), 1820–1843. doi:10.1111/maps.13181

- Castillo-Rogez, J.C., & Rayman, M. D. (2020) A bountiful harvest on Ceres. *Nature Astronomy*, 4, 807. doi: 10.1038/s41550-020-1031-5
- Coleyshaw, E. E., Crump, G., & Griffith, W. P. (2003). Vibrational spectra of the hydrated carbonate minerals ikaite, monohydrocalcite, lansfordite and nesquehonite. *Spectrochimica Acta Part A: Molecular and Biomolecular Spectroscopy*, 59(10), 2231–2239. doi:10.1016/S1386-1425(03)00067-2
- Cox, G. F. N., & Weeks, W. F. (1975). Brine drainage and initial salt entrapment in sodium chloride ice. *CRREL Report*, 345, 85. Hanover, NH: U.S. Army Cold Regions Research and Engineering Laboratory.
- Cox, G. F. N., & Weeks, W. F. (1986). Changes in the salinity and porosity of sea-ice samples during shipping and storage. *Journal of Glaciology*, 32(112), 371–375. doi:10.3189/S0022143000012065
- Cox, G. F. N., & Weeks, W. F. (1988). Numerical simulations of the profile properties of undeformed first-year sea ice during growth season. *Journal of Geophysical Research: Oceans*, 93(C10), 12449–12460. doi:10.1029/JC093iC10p12449
- Culha, C., & Manga, M. (2016). Geometry and spatial distribution of lenticulae on Europa. *Icarus*, 271, 49–56. doi:10.1016/j.icarus.2015.12.052
- Davaa, G., Oyunbaatar, D., & Sugita, M. (2007). Surface water in Mongolia. In Y. Konagaya (Ed.), *A Handbook of Mongolian Environments*, 55–68. Kyoto, Japan: Kenbunsha.
- De Sanctis, M. C., Ammannito, E., Raponi, A., Marchi, S., McCord, T. B., McSween, H. Y., Capaccioni, F., Capria, M. T., Carrozzo, F. G., Ciarniello, M., Longobardo, A., Tosi, F., Fonte, S., Formisano, M., Frigeri, A., Giardino, M., Magni, G., Palomba, E., Turrini, D., Zambon, F., Combe, J.-P., Feldman, W., Jaumann, R., McFadden, L. A., Pieters, C. M., Prettyman, T., Toplis, M., Raymond, C. A., & Russell, C. T. (2015). Ammoniated phyllosilicates with a likely outer Solar System origin on (1) Ceres. *Nature* 528, 241–244. doi:10.1038/nature16172
- De Sanctis, M. C., Raponi, A., Ammannito, E., Ciarniello, M., Toplis, M. J., McSween, H. Y., Castillo-Rogez, J. C., Ehlmann, B. L., Carrozzo, F. G., Marchi, S., Tosi, F., Zambon, F., Capaccioni, F., Capria, M. T., Fonte, S., Formisano, M., Frigeri, A., Giardino, M., Longobardo, A., Magni, G., Palomba, E., McFadden, L. A., Pieters, C. M., Jaumann, R., Schenk, P., Mugnuolo, R., Raymond, C. A., & Russell, C. T. (2016). Bright carbonate deposits as evidence of aqueous alteration on (1) Ceres. *Nature*, 536, 54–57. doi:10.1038/nature18290
- De Sanctis, M. C., Ammannito, E., Raponi, A., Frigeri, A., Ferrari, M., Carrozzo, F. G., Ciarniello, M., Formisano, M., Rousseau, B., Tosi, F., Zambon, F., Raymond, C. A., & Russell, C. T. (2020a). Fresh emplacement of hydrated sodium chloride on Ceres

- from ascending salty fluids. *Nature Astronomy*, 4, 786–793. doi:10.1038/s41550-020-1138-8
- De Sanctis, M. C., Mitri, G., Castillo-Rogez, J., House, C. H., Marchi, S., Raymond, C. A., & Sekine, Y. (2020b). Relict ocean worlds: Ceres. *Space Science Reviews*, 216(60), 1–33. doi:10.1007/s11214-020-00683-w
- Desch, S. J., Cook, J. C., Doggett, T. C., & Porter, S. B. (2009). Thermal evolution of Kuiper belt objects, with implications for cryovolcanism. *Icarus*, 202(2), 694–714. doi: 10.1016/j.icarus.2009.03.009
- Dionne, J. (1979). Ice action in the lacustrine environment. A review with particular reference to subarctic Quebec, Canada. *Earth-Science Reviews*, 15(3), 185–212. doi: /10.1016/0012-8252(79)90082-5
- Evans, R. J., & Untersteiner, N. (1971). Thermal cracks in floating ice sheets. *Journal of Geophysical Research: Oceans and Atmospheres*, 76(3), 694–703. doi:10.1029/JC076i003p00694
- Ermakov, A. I., Fu, R. R., Castillo-Rogez, J. C., Raymond, C. A., Park, R. S., Preusker, F., Russell, C. T., Smith, D. E., & Zuber, M. T. (2017). Constraints on Ceres' internal structure and evolution from its shape and gravity measured by the Dawn spacecraft. *Journal of Geophysical Research: Planets*, 122, 2267–2293. doi: 10.1002/2017JE005302
- Fagents, S. A. (2003). Considerations for effusive cryovolcanism on Europa: The post-Galileo perspective. *Journal of Geophysical Research: Planets*, 108(E12), 5139. doi:10.1029/2003JE002128
- Fagents, S. A., Greeley, R., Sullivan, R. J., Pappalardo, R. T., Prockter, L. M., & The Galileo SSI Team. (2000). Cryomagmatic Mechanisms for the Formation of Rhadamanthys Linea, Triple Band Margins, and Other Low-Albedo Features on Europa. *Icarus* 144, 54–88. doi:10.1006/icar.1999.6254
- Fortes, A. D., Grindrod, P. M., Trickett, S. K., & Voadlo, L. (2007). Ammonium sulfate on Titan: Possible origin and role in cryovolcanism. *Icarus* 188, 139–153. doi: 10.1016/j.icarus.2006.11.002
- Fox-Powell, M. G., & Cousins, C. R. (2021). Partitioning of crystalline and amorphous phases during freezing of simulated Enceladus ocean fluids. *Journal of Geophysical Research: Planets*, 126, e2020JE006628. doi: 10.1029/2020JE006628
- Fukushi, K., Suzuki, Y., Kawano, J., Ohno, T., Ogawa, M., Yaji, T., & Takahashi, Y. (2017). Speciation of magnesium in monohydrocalcite: XANES, ab initio and geochemical modeling. *Geochimica et Cosmochimica Acta*, 213, 457–474. doi:10.1016/j.gca.2017.06.040
- Fukushi, K., & Matsumiya, H. (2018). Control of water chemistry in alkaline lakes: solubility of monohydrocalcite and amorphous magnesium carbonate in CaCl<sub>2</sub>–MgCl<sub>2</sub>–Na<sub>2</sub>CO<sub>3</sub> solutions. *ACS Earth Space Chemistry* 2(7), 735–744.

doi:10.1021/acsearthspacechem.8b00046

- Fukushi, K., Sekine, Y., Sakuma, H., Morida, K., & Wordsworth, R. (2019). Semiarid climate and hyposaline lake on early Mars inferred from reconstructed water chemistry at Gale. *Nature Communications*, 10, 4896. doi:10.1038/s41467-019-12871-6
- Fukushi, K., Imai, E., Sekine, Y., Kitajima, T., Gankhurel, B., Davaasuren, D., & Hasebe, N. (2020). In situ formation of monohydrocalcite in alkaline saline lakes of the Valley of Gobi Lakes: Prediction for Mg, Ca, and total dissolved carbonate concentrations in Enceladus' ocean and alkaline-carbonate ocean worlds. *Minerals*, 10(8), 669. doi:10.3390/min10080669
- Glein, C. R., Baross, J. A., & Waite, J. H. (2015). The pH of Enceladus' ocean. *Geochimica et Cosmochimica Acta*, 162, 202-219. doi: 10.1016/j.gca.2015.04.017
- Gross, G. W., Wong, P. M., & Humes, K. (1977). Concentration dependent solute redistribution at the ice-water phase boundary. III. Spontaneous convection. Chloride solutions. *The Journal of Chemical Physics*, 67, 5264-5274. doi:10.1063/1.434704
- Hand, K. P., & Carlson, R. W. (2015). Europa's surface color suggests an ocean rich with sodium chloride. *Geophysical Research Letters*, 42(9), 3174-3178. doi:10.1002/2015GL063559
- Head III, J. W., & Pappalardo, R. T. (1999). Brine mobilization during lithospheric heating on Europa: Implications for formation of chaos terrain, lenticula texture, and color variations. *Journal of Geophysical Research*, 104(E11), 27143-27156. doi:10.1029/1999JE001062
- Hussmann, H., & Spohn, T. (2004). Thermal-orbital evolution of Io and Europa. *Icarus*, 171, 2, 391-410. doi: 10.1016/j.icarus.2004.05.020.
- Johnson, P. V., Hodyss, R., Vu, T. H., & Choukroun, M. (2019). Insights into Europa's ocean composition derived from its surface expression. *Icarus*, 321, 857-865. doi: 10.1016/j.icarus.2018.12.009
- Jones, B. F., Eugster, H. P., & Rettig, S. L. (1977). Hydrochemistry of the Lake Magadi basin, Kenya. *Geochimica et Cosmochimica Acta*, 41(1), 53-72. doi: 10.1016/0016-7037(77)90186-7
- Kamata, S., Nimmo, F., Sekine, Y., Kuramoto, K., Noguchi, N., Kimura, J., & Tani, A. (2019). Pluto's ocean is capped and insulated by gas hydrates. *Nature Geoscience*, 12, 407-410. doi: 10.1038/s41561-019-0369-8
- King, T. V. V., Clark, R. N., Calvin, W. M., Sherman, D. M., & Brown, R. H. (1992). Evidence for ammonium-bearing minerals on Ceres. *Science*, 255 (5051), 1551-1553. doi: 10.1126/science.255.5051.1551
- Kitajima, T., Fukushi, K., Yoda, M., Takeichi, Y., & Takahashi, Y. (2020). Simple, reproducible synthesis of pure monohydrocalcite with low Mg content. *Minerals*, 10(4), 346. doi:10.3390/min10040346

- Klug, H. P., & Alexander, L. E. (1973). *X-ray Diffraction Procedures for Polycrystalline and Amorphous Materials*. Plenum Press, New York.
- Kurokawa, H., Shibuya, T., Sekine, Y., Ehlmann, B. L., Usui, F., Kikuchi, S., & Yoda, M. (2021). Distant formation and differentiation of outer main belt asteroids and carbonaceous chondrite parent bodies. *AGU Advance*. doi: 10.1029/2021AV000568
- Lesage, E., Massol, H., & Schmidt, F. (2020). Cryomagma ascent on Europa. *Icarus*, 335, 113369. doi:10.1016/j.icarus.2019.07.003
- Lofgren, G., & Weeks, W. (1969). Effect of growth parameters on substructure spacing in NaCl ice crystals. *Journal of Glaciology*, 8(52), 153–164. doi:10.3189/S0022143000020827
- Manga, M., & Michaut, C. (2017). Formation of lenticulae on Europa by saucer-shaped sills. *Icarus*, 286, 261–269. doi:10.1016/j.icarus.2016.10.009
- Manga, M., & Wang, C. Y. (2007). Pressurized oceans and the eruption of liquid water on Europa and Enceladus. *Geophysical Research Letters*, 34(7), L07202. doi:10.1029/2007GL029297
- Marion, G. M., Mironenko, M. V., & Roberts, M. V. (2010). FREZCHEM: A geochemical model for cold aqueous solutions. *Computers & Geosciences*, 36(1), 10–15. doi:10.1016/j.cageo.2009.06.004
- Mironenko, M. V., Grant, S. A., Marion, G. M., & Farren, R. E. (1997). FREZCHEM2: a chemical thermodynamic model for electrolyte solutions at subzero temperatures. *CRREL Report*, 97–5. Hanover, NH: U.S. Army Cold Regions Research and Engineering Laboratory.
- Morishige, Y., & Kimura, A. (2008). Ionization interference in inductively coupled plasma-optical emission spectrometry. *Sei Technical Review*, 66, 106–111.
- Munemoto, T., & Fukushi, K. (2011). Solubility of monohydrocalcite. Kanazawa, Japan: Institute of Nature and Environmental Technology, Kanazawa University.
- Nagashima, K., & Furukawa, Y. (2000). Time development of a solute diffusion field and morphological instability on a planar interface in the directional growth of ice crystals. *Journal of Crystal Growth*, 209(1), 167–174. doi:10.1016/S0022-0248(99)00511-4
- Nakawo, M., & Sinha, N. K. (1981). Growth rate and salinity profile of first-year sea ice in the high Arctic. *Journal of Glaciology*, 27(96), 315–330. doi:10.3189/S0022143000015409

- Nathues, A., Hoffmann, M., Platz, T., Thangjam, G. S., Cloutis, E. A., Reddy, V., Le Corre, L., Li, J.-Y., Mengel, K., Rivkin, A., Applin, D.M., Schaefer, M., Christensen, U., Sierks, H., Ripken, J., Schmidt, B. E., Hiesinger, H., Sykes, M. V., Sizemore, H. G., Preusker, F. & Russell, C.T. (2016). FC colour images of dwarf planet Ceres reveal a complicated geological history. *Planetary and Space Science*, 134, 122-127. doi: 10.1016/j.pss.2016.10.017
- Nathues, A., Platz, T., Hoffmann, M., Thangjam, G., Cloutis, E. A., Applin, D. M., Le Corre, L., Reddy, V., Mengel, K., Protopapa, S., Takir, D., Preusker, F., Schmidt, B. E., & Russell, C. T.(2017). Oxo Crater on (1) Ceres: Geological History and the Role of Water-ice. *The Astronomical Journal*, 154, 3. Doi: 10.3847/1538-3881/aa7a04
- Nathues, A., Schmedemann, N., Thangjam, G., Pasckert, J. H., Mengel, K., Castillo-Rogez, J., Cloutis, E. A., Hiesinger, H., Hoffmann, M., Le Corre, L., Li, J.-Y., Pieters, C., Raymond, C. A., Reddy, V., Ruesch O., & Williams, D. A. (2020). Recent cryovolcanic activity at Occator crater on Ceres. *Nature Astronomy*, 4, 794–801. doi:10.1038/s41550-020-1146-8
- Neveu, M., & Desch, S. J. (2015). Geochemistry, thermal evolution, and cryovolcanism on Ceres with a muddy ice mantle. *Geophysical Research Letters*, 42(23), 10197–10206. doi:10.1002/2015GL066375
- Pappalardo, R. T., & Barr, A. C. (2004). The origin of domes on Europa: The role of thermally induced compositional diapirism. *Geophysical Research Letters*, 31(1), L01701. doi:10.1029/2003GL019202
- Park, R., Konopliv, A., Bills, B., Rambaux, N., Castillo-Rogez, J. C., Raymond, C. A., Vaughan, A. T., Ermakov, A. I., Zuber, M. T., Fu, R. R., Toplis, M. J., Russell, C. T., Nathues, A., & Preusker, F. (2016). A partially differentiated interior for (1) Ceres deduced from its gravity field and shape. *Nature* 537, 515–517. doi:10.1038/nature18955
- Parmeter, R. R., & Coon, M. D. (1972). Model of pressure ridge formation in sea ice. *Journal of Geophysical Research*, 77(33), 6565-6575. doi: 10.1029/JC077i033p06565
- Raymond, C. A., Ermakov, A. I., Castillo-Rogez, J. C., Marchi, S., Johnson, B. C., Hesse, M. A., Scully, J. E. C., Buczkowski, D. L., Sizemore, H. G., Schenk, P. M., Nathues, A., Park, R. S., Prettyman, T. H., Quick, L. C., Keane, J. T., Rayman M. D., & Russell, C. T. (2020). Impact-driven mobilization of deep crustal brines on dwarf planet Ceres. *Nature Astronomy*, 4, 741–747. doi:10.1038/s41550-020-1168-2
- Quick, L. C., Buczkowski, D. L., Ruesch, O., Scully, J. E. C., Castillo-Rogez, J., Raymond, C. A., Schenk, P. M., Sizemore, H. G., & Sykes, M. V. (2019). A Possible Brine Reservoir Beneath Occator Crater: Thermal and Compositional Evolution and Formation of the Cerealia Dome and Vinalia Faculae. *Icarus*, 320, 119-135. doi: 10.1016/j.icarus.2018.07.016.

- Rivkin, A. S., Volquardsen, E. L., & Clark, B. E. (2006). The surface composition of Ceres: Discovery of carbonates and iron-rich clays. *Icarus*, 185 (2), 563–567. doi: 10.1016/j.icarus.2006.08.022
- Rivkin, A. S., & Volquardsen, E. L. (2010). Rotationally-resolved spectra of Ceres in the 3- $\mu$ m region. *Icarus*, 206, 1, 327-333. doi:10.1016/j.icarus.2009.08.026
- Ruesch, O., Platz, T., Schenk, P., McFadden, L. A., Castillo-Rogez, J. C., Quick, L. C., Byrne, S., Preusker, F., O'Brien, D. P., Schmedemann, N., Williams, D. A., Li, J.-Y., Bland, M. T., Hiesinger, H., Kneissl, T., Neesemann, A., Schaefer, M., Pasckert, J. H., Schmidt, B. E., Buczkowski, D.L., Sykes, M.V., Nathues, A., Roatsch, T., Hoffmann, M., Raymond, C. A., & Russell, C. T. (2016). Cryovolcanism on Ceres. *Science*, 353, 6303, aaf4286. doi: 10.1126/science.aaf4286
- Ruesch, O., Genova, A., Neumann, W., Quick, L. C., Castillo-Rogez, J. C., Raymond, C. A., Russell, C. T., & Zuber, M. T. (2019a). Slurry extrusion on Ceres from a convective mud-bearing mantle. *Nature Geoscience*, 12, 505–509. doi: 10.1038/s41561-019-0378-7
- Ruesch, O., Quick, L. C., Landis, M. E., Sori, M. M., Čadek, O., Brož, P., Otto, K. A., Bland, M. T., Byrne, S., Castillo-Rogez, J. C., Hiesinger, H., Jaumann, R., Krohn, K., McFadden, L. A., Nathues, A., Neesemann, A., Preusker, F., Roatsch, T., Schenk, P. M., Scully, J. E. C., Sykes, M. V., Williams, D. A., Raymond, C. A., & Russell, C.T. (2019b). Bright carbonate surfaces on Ceres as remnants of salt-rich water fountains. *Icarus*, 320, 39-48. doi:10.1016/j.icarus.2018.01.022.
- Russell, C. T., & Raymond, C. A. (2012). *The Dawn Mission to Minor Planets 4 Vesta and 1 Ceres*. Springer-Verlag: New York. doi: 10.1007/978-1-4614-4903-4
- Sekine, Y., Kitajima, T., Fukushi, K., Gankhurel, B., Tsetsgee, S., Davaasuren, D., Matsumiya, H., Chida, T., Nakamura, M., & Hasebe, N. (2020). Hydrogeochemical study on closed-basin lakes in cold and semi-arid climates of the Valley of the Gobi Lakes, Mongolia: Implications for hydrology and water chemistry of paleolakes on Mars. *Minerals*, 10(9), 792. doi:10.3390/min10090792
- Strub-Klein, L., & Sudom, D. (2012). A comprehensive analysis of the morphology of first-year sea ice ridges. *Cold Regions Science and Technology*, 82, 94–109. doi: 10.1016/j.coldregions.2012.05.014.
- Scully, J. E. C., Baker, S. R., Castillo-Rogez, J. C & Buczkowski, D. L. (2021). The In Situ Exploration of a Relict Ocean World: An Assessment of Potential Landing and Sampling Sites for a Future Mission to the Surface of Ceres. *The Planetary Science Journal*, 2, 3. doi: 10.3847/PSJ/abee28
- Szumińska, D. (2016). Changes in surface area of the Böön Tsagaan and Orog lakes (Mongolia, Valley of the Lakes, 1974–2013) compared to climate and permafrost changes. *Sedimentary Geology*, 340, 62–73. doi:10.1016/j.sedgeo.2016.03.002

- Tan, S., Sekine, Y., Shibuya, T., Miyamoto, C., & Takahashi, Y. (2021). The role of hydrothermal sulfate reduction in the sulfur cycles within Europa: Laboratory experiments on sulfate reduction at 100 MPa. *Icarus*, 357, 114222. doi:10.1016/j.icarus.2020.114222
- Tanaka, J., Kawano, J., Nagai, T., & Teng, H. (2019). Transformation process of amorphous magnesium carbonate in aqueous solution. *Journal of Mineralogical and Petrological Sciences*, 114(2), 105–109. doi:10.2465/jmps.181119b
- Thomas, E. C., Hodyss, R., Vu, T. H., Johnson, P. V., & Choukron, M. (2017). Composition and evolution of frozen chloride brines under the surface conditions of Europa. *ACS Earth Space Chemistry*, 1(1), 14–23. doi:10.1021/acsearthspacechem.6b00003
- Thomas, C., Vu, T. H., Hodyss, R., Johnson, P. V., & Choukron, M. (2019). Kinetic effect on the freezing of ammonium-sodium-carbonate-chloride brines and implications for the origin of Ceres' bright spots. *Icarus*, 320, 150-158. doi: 10.1016/j.icarus.2017.12.038
- Vitagliano, V., & Lyons, P. A. (1956). Diffusion Coefficients for Aqueous Solutions of Sodium Chloride and Barium Chloride. *Journal of the American Chemical Society*, 78 (8), 1549–1552. doi: 10.1021/ja01589a011
- Vu, T. H., Hodyss, R., Choukron, M., & Johnson, P. V. (2016). Chemistry of frozen sodium–magnesium–sulfate–chloride brines: Implications for surface expression of Europa's ocean composition. *The Astrophysical Journal Letters*, 816(2), L26. doi:10.3847/2041-8205/816/2/L26
- Waite Jr, J. H., Lewis, W. S., Magee, B. A., Lunine, J. I., McKinnon, W. B., Glein, C. R., Mousis, O., Young, D. T., Brockwell, T., Westlake, J., Nguyen, M. J., Teolis, B. D., Niemann, H. B., McNutt Jr, R. L., Perry, M., & Ip, W. H. (2009). Liquid water on Enceladus from observations of ammonia and <sup>40</sup>Ar in the plume. *Nature* 460, 487–490. doi: 10.1038/nature08352
- Weeks, W. F., & Lofgren, G. (1967). The effective solute distribution coefficient during the freezing of NaCl solutions. In H. Oura (Eds.), *Physics of Snow and Ice*, International Conference on Low Temperature Science, Proceedings, 1(1), 579–597.
- Yavuz, A. A., Phoenix, S. L., & TerMaath, S. C. (2006). An accurate and fast analysis for strongly interacting multiple crack configurations including kinked (V) and branched (Y) cracks. *International Journal of Solids and Structures*, 43(22–23), 6727–6750. doi:10.1016/j.ijsolstr.2006.02.005
- Yoda, M., Sekine, Y., Fukushi, F., Kitajima, T., Gankhurel, B., Davaasuren, D., Gerelmaa, T., Ganbat, S., Shoji, D., Zolotov, M. Y., & Takahashi, Y. (2021). Field Investigations of Chemical Partitioning and Aqueous Chemistry of Freezing Closed-Basin Lakes in Mongolia as Analogs of Subsurface Brines on Icy Bodies. *Journal of Geophysical Research: Planets*, 126, e2021JE006972. doi: 10.1029/2021JE006972

Zambon, F., Raponi, A., Tosi, F., De Sanctis, M. C., McFadden, L. A., Carrozzo, F. G., Longobardo, A., Ciarniello, M., Krohn, K., Stephan, K., Palomba, E., Pieters, C. M., Ammannito, E., Russell, C. T., & Raymond C. A. (2017). Spectral analysis of Ahuna Mons from Dawn mission's visible-infrared spectrometer. *Geophysical Research Letters*, 44, 97–104. doi:10.1002/2016GL071303.

Zolotov, M. (2007). An oceanic composition on early and today's Enceladus. *Geophysical Research Letters*, 34, L23203. doi:10.1029/2007GL031234

Zolotov, M. Y., & Kargel, J. (2009). On the Chemical Composition of Europa's Icy Shell, Ocean, and Underlying Rocks. In R. T. Pappalardo, W. B. McKinnon, K. K. Khurana (Eds.), *Europa* (pp. 431–457). Tucson, AZ: University of Arizona Press.

Zolotov, M. (2012). Aqueous fluid composition in CI chondritic materials: Chemical equilibrium assessments in closed systems. *Icarus*, 220(2), 713–729. doi: 10.1016/j.icarus.2012.05.036.

Zolotov, M. (2017). Aqueous origins of bright salt deposits on Ceres. *Icarus*, 296, 289–304. doi:10.1016/j.icarus.2017.06.018

## Appendix A

In Appendix A, supplemental information of Chapter 3 was provided. Fig. A1 shows close-up images of whitish ice veins (wet cracks) on Orog lake, found in our field survey in 2020. Fig. A2 shows the vertical distribution of salinity in ice samples collected during the field survey of February 2019 (samples Olgoy\_2019C1, Orog\_2019W1, and Orog\_2019W2). For Orog\_2019W1, charge balance conditions between cations and anions were not satisfied at the three shallowest depths (5, 15, and 25 cm). Fig. A3 shows Ca K-edge X-ray absorption near-edge structure spectra (4030–4070 eV) of the solid residues after freeze-drying Orog\_2019W1. Standard spectra for calcite, aragonite, and dolomite were taken from Takahashi et al. (2008). Fig. A4 shows the calculated chemical evolution of lake bottom-water for Runs #1–8 for Olgoy and Orog lakes (i.e., the concentrations, precipitated minerals, and pH values). Table A1 lists the measured compositions of lake water from Olgoy and Orog lakes during summer 2018. The saturation indexes (SIs), except those for monohydrocalcite (MHC) and amorphous Mg-carbonate (AMC), were obtained using the solution equilibrium software Visual MINTEQ ver. 3.1. The SIs of MHC and AMC were obtained using the solution equilibrium software Geochemist's Workbench. Total salinity was calculated based on the concentrations of major ions (i.e., Na, K, Mg, Ca, Cl, and  $\text{SO}_4^{2-}$ ). Table A2 presents the sampling information for the field surveys in January 2020 and February 2019. Ice thickness and ice sampling depth were measured during drilling. The bottom water thickness was defined as the length from the ice surface to the top of the sediment layer. Table A3 presents the solution chemistries of lake bottom-water collected from Olgoy and Orog lakes in January 2020. Table A4 summarizes the minerals, dissolved species, and gas species considered in the model calculations using the FREZCHEM software.

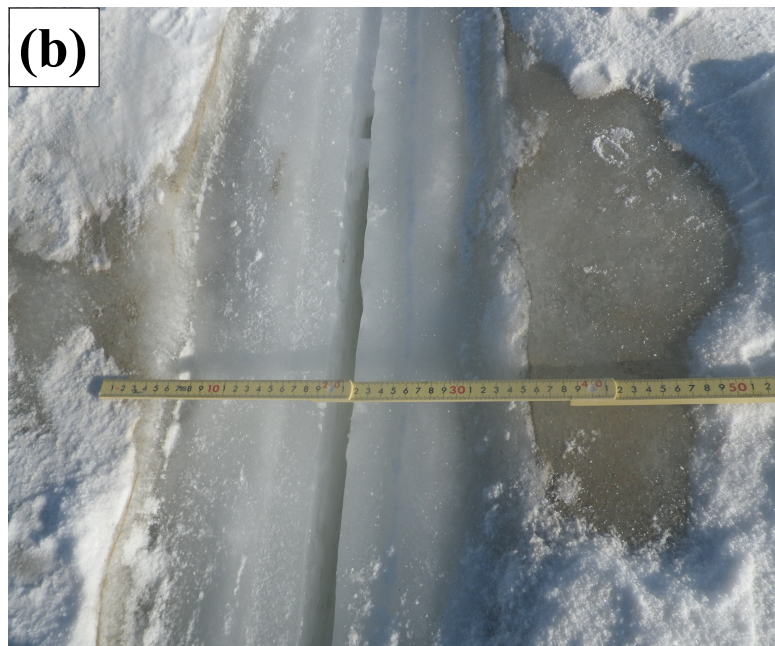
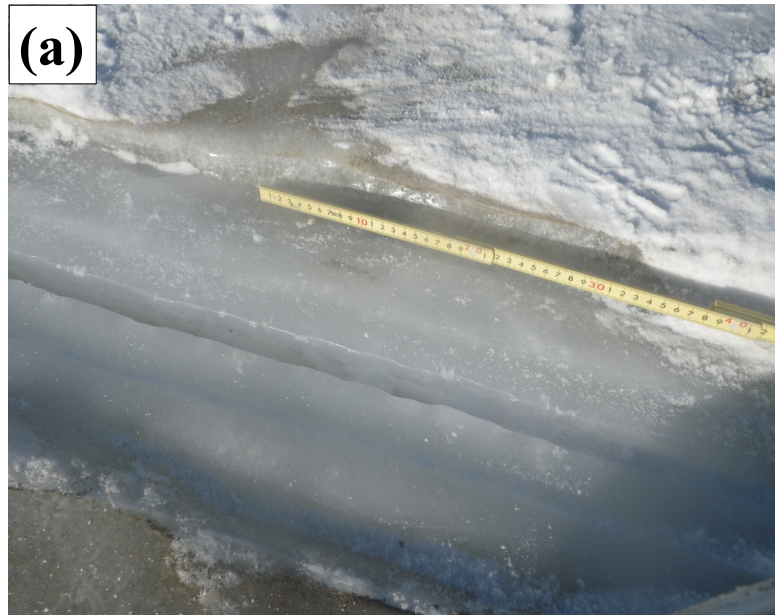


**Figure A1. Close-up images of whitish ice veins (wet cracks) found in Orog lake during the survey in 2020 (a, b). The unit in the scale in the images is centi-meter.**

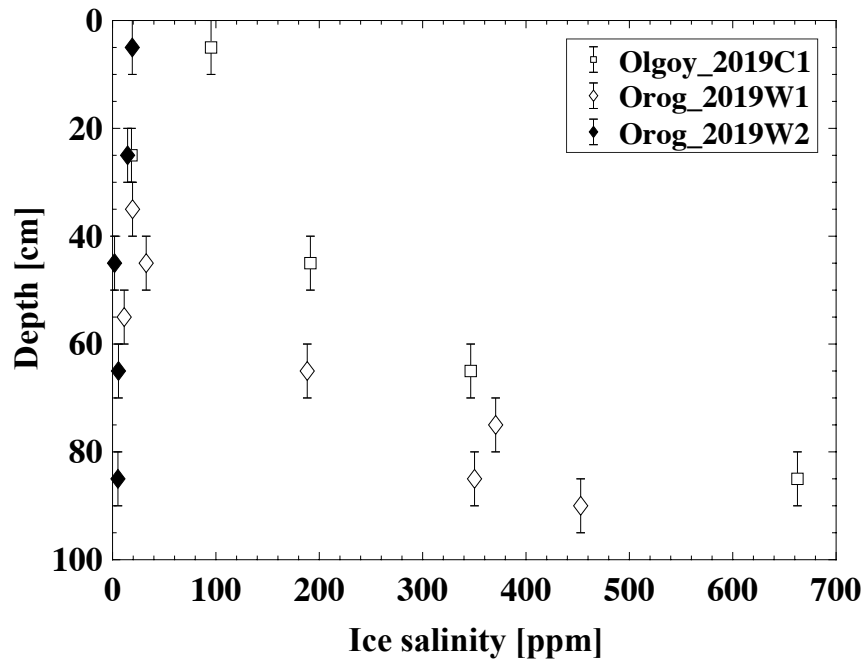
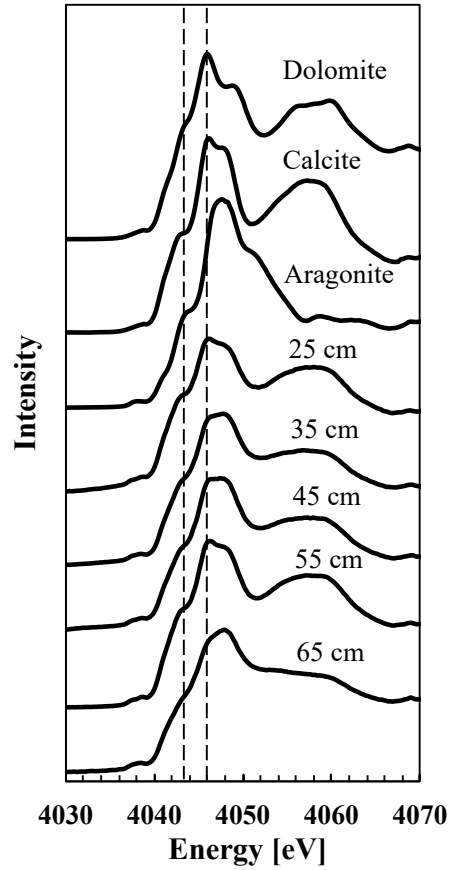


Figure A2. Salinity profiles of ice samples analyzed by ICP-OES and ion chromatography for Olgoy\_2019C1, Orog\_2019W1, and Orog\_2019W2.



**Figure A3. Ca K-edge X-ray absorption near-edge structure spectra (4030–4070 eV) of ice samples from Orog\_2019C1. Depths of the ice samples are shown in the figure. Broken vertical lines at 4043.5 and 4046 eV are the pre-edge peak and peak of calcite, respectively.**

(a) Olgoy Lake (Runs #1–#8)

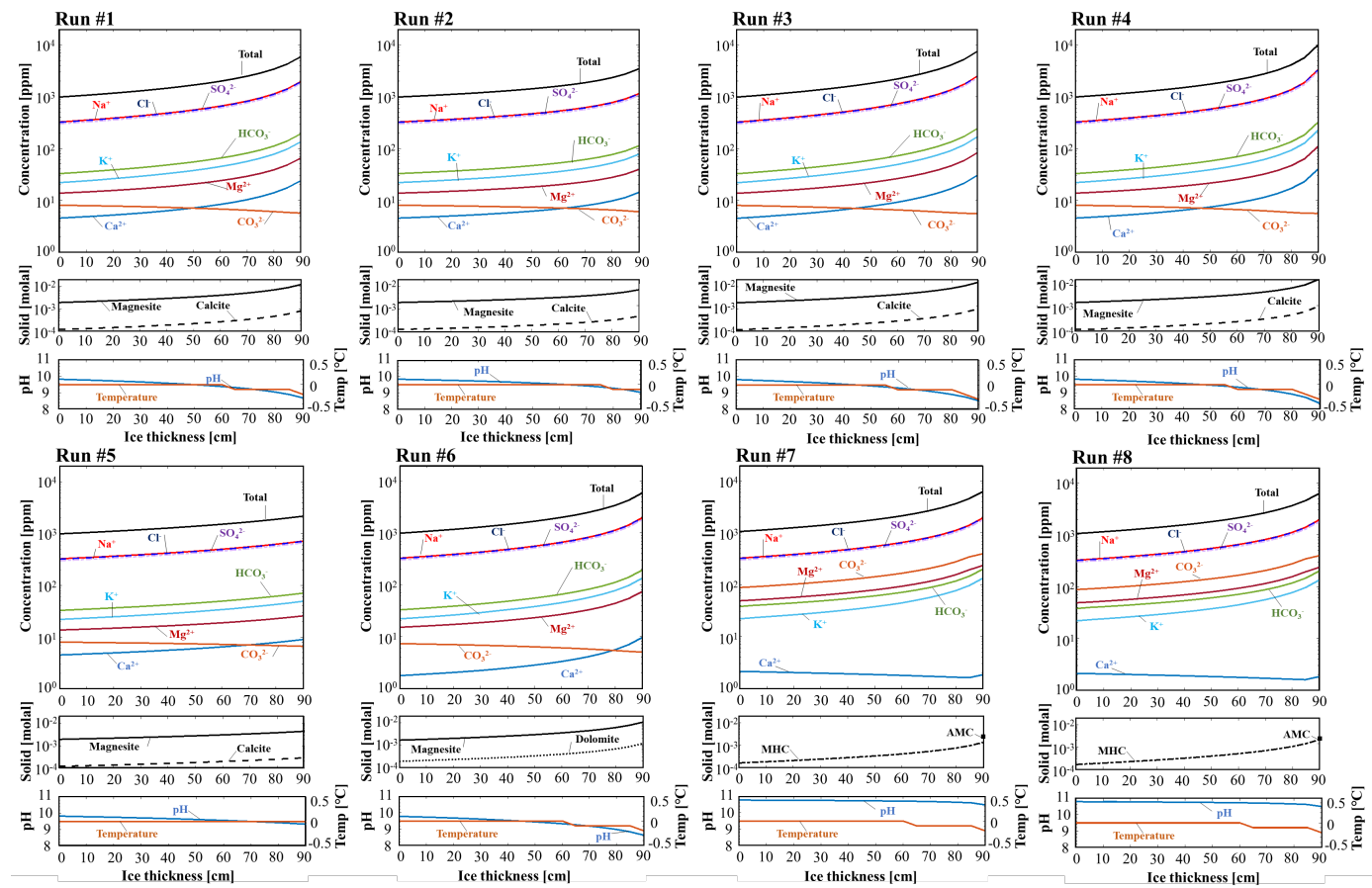


Figure A4. Model results of the chemical evolution of the lake bottom-water (concentration, precipitated minerals, and pH). (a) Olgoy Lake (Runs #1–#8); (b) Western Orog Lake (Runs #1–#8); (c) Central Orog Lake (Runs #1–#8).

**(b) Western Orog Lake (Runs #1–#8)**

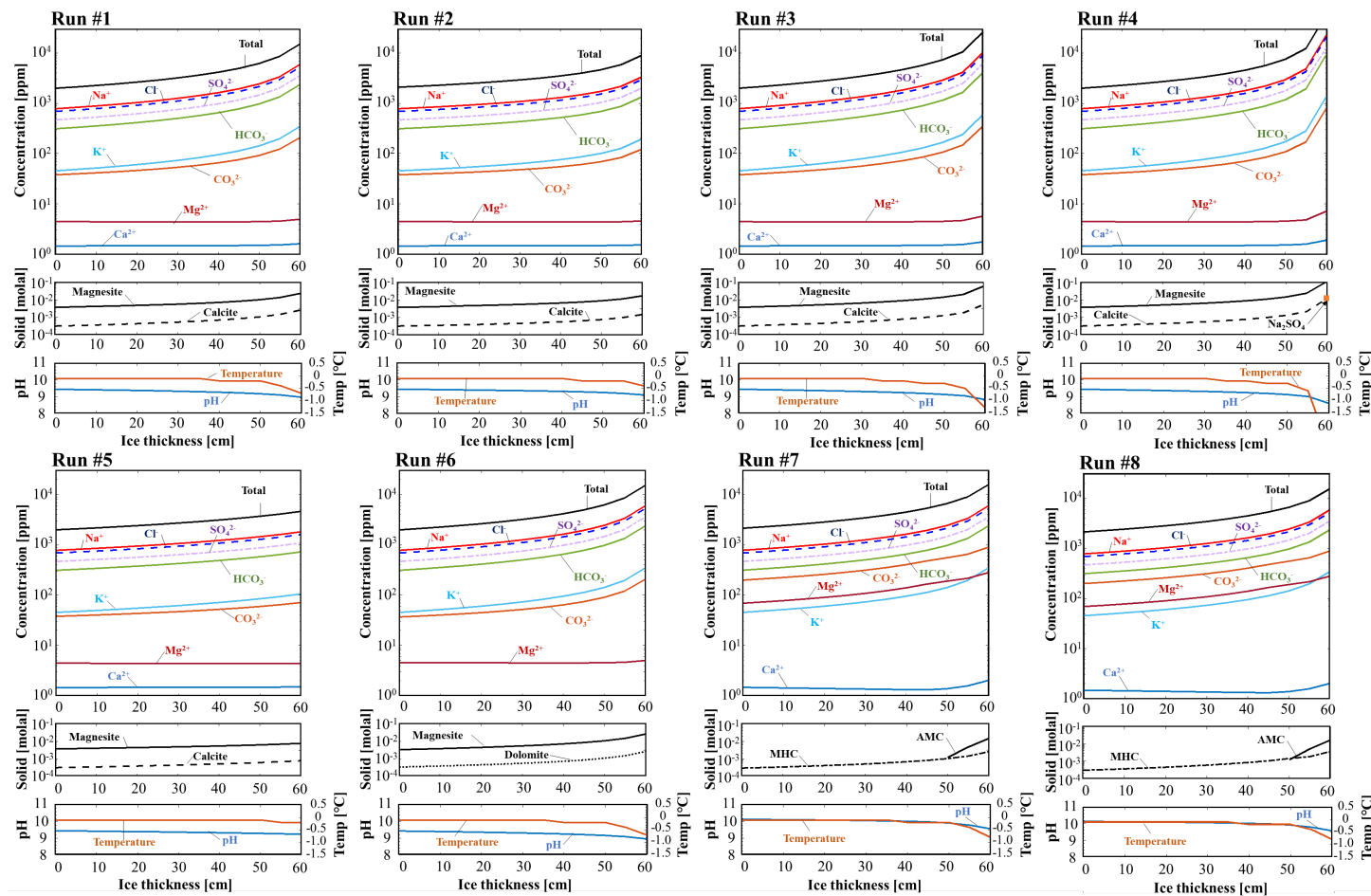


Figure A4. Continued.

(c) Central Orog Lake (Runs #1–#8)

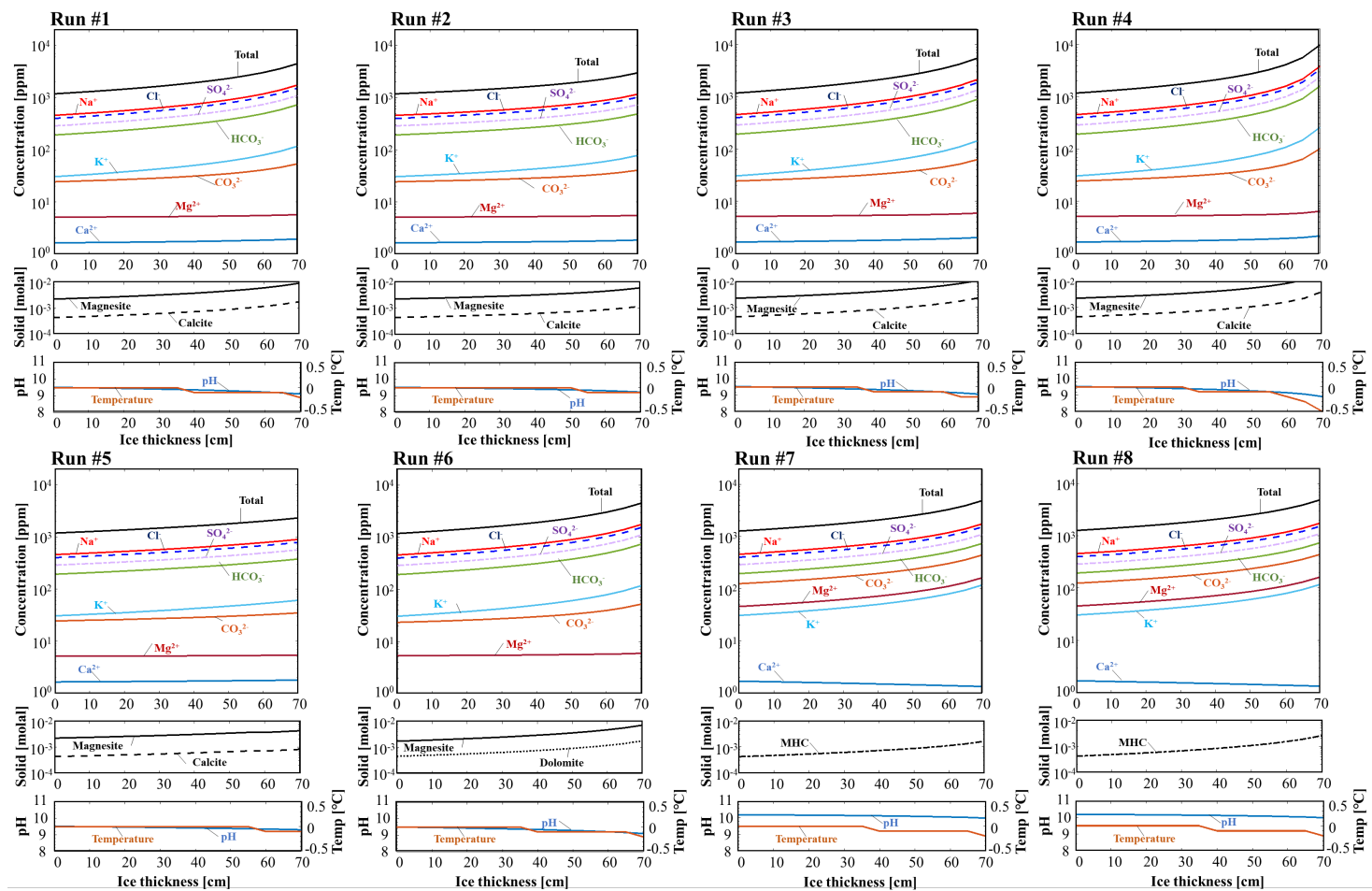


Figure A4. Continued.

**Table A1. Physical and chemical data for lake water from Orog and Olgoy lakes during summer 2018.**

\*The saturation index (SI) was obtained at 0°C.

Lake	Olgoy Lake	Western Orog Lake	Central Orog Lake
Sampling date	24 August 2018	28 August 2018	28 August 2018
Sampling depth	Surface	Surface	Surface
Na (ppm)	326	782	458
K (ppm)	22	45	30
Mg (ppm)	61	93	59
Ca (ppm)	10	14	19
Cl (ppm)	320	691	399
SO <sub>4</sub> (ppm)	301	470	288
Salinity (ppm)*	1,040	2,095	1,253
Alkalinity (mEq/L)	17.1	15.4	10.2
pH	9.53	9.12	9.14
EC (mS/m)	244	434	266
DO (mg/L)	7.6	7.12	5.78
ORP (mV)	109	92	99
Temperature (°C)	11.5	21.9	21.8
Saturation index (SI) of monohydrocalcite (MHC) (CaCO <sub>3</sub> ·H <sub>2</sub> O)**	0.385	0.462	0.361
SI of halite (NaCl)**	-5.547	-4.911	-5.355
SI of thenardite (Na <sub>2</sub> SO <sub>4</sub> )**	-7.049	-6.197	-6.786

**Table A2. Sampling details of the field surveys in January 2020 and February 2019.**

\* Locations where remaining lake bottom-water samples were collected.

Sample name and location	Latitude	Longitude	Lake	Sampling date	Ice thickness [cm]	Bottom water thickness [cm]	Sampling depth [cm]
Olgoy_2020C1	46° 33'42.9"	100° 06'33.6"	Olgoy	17 Jan. 2020	90	130*	5, 15, 25, 35, 45, 55, 65, 75, 85
Olgoy_2020C1-crack	46° 33'42.9"	100° 06'33.6" 100° 34'50.6"	Olgoy	17 Jan. 2020	95	130	5, 15, 25, 35, 45, 55, 65, 75, 85, 95
Olgoy_2020C2	46° 33'41.9"	100° 06'38.3"	Olgoy	17 Jan. 2020	100	150*	5, 35, 55, 75, 95
Olgoy_2020N1	46° 34'22.3"	100° 06'39.8"	Olgoy	17 Jan. 2020	85	85	5, 25, 45, 65, 85
Olgoy_2020S1	46° 33'14.9"	100° 05'57.1"	Olgoy	17 Jan. 2020	70	70	5, 15, 25, 35, 45, 55
Olgoy_2020S2	46° 33'01.6"	100° 05'35.3"	Olgoy	17 Jan. 2020	60	60	5, 25, 35, 45, 55
Olgoy_2019C1	46° 33'52.5"	100° 06'26.4"	Olgoy	12 Feb. 2019	90	90	5, 15, 35, 55, 75
Orog_2020W1	45° 03'55.9"	100° 34'29.4"	Orog (west)	19 Jan. 2020	60	80*	5, 15, 25, 35, 45, 55
Orog_2020W2	45° 04'00.2"	100° 34'12.3"	Orog (west)	20 Jan. 2020	60	60	5, 15, 25, 35, 45, 55
Orog_2020W2-crack1	45° 04'00.2"	100° 34'12.3"	Orog (west)	20 Jan. 2020	60	60	5, 15, 25, 35, 45, 55
Orog_2020W2-crack2	45° 04'00.2"	100° 34'12.3"	Orog (west)	20 Jan. 2020	60	60	5, 15, 25, 35, 45, 55
Orog_2020C1	45° 03'48.4"	100° 39'04.1"	Orog (central)	19 Jan. 2020	65	105*	5, 25, 35, 45, 55
Orog_2020C2	45° 03'38.4"	100° 41'44.8"	Orog (central)	19 Jan. 2020	65	105*	5, 25, 45, 55
Orog_2020C3	45° 03'33.6"	100° 45'56.0"	Orog (central)	19 Jan. 2020	70	120*	5, 15, 25, 35, 45, 55, 65
Orog_2020C4	45° 02'19.8"	100° 41'54.1"	Orog (central)	19 Jan. 2020	75	125	5, 15, 25, 45, 55, 65
Orog_2020C5	45° 02'45.9"	100° 38'35.8"	Orog (central)	19 Jan. 2020	70	110	5, 25, 45, 55, 65
Orog_2019W1	45° 04'04.1"	100° 33'54.8"	Orog (west)	14 Feb. 2019	90	100*	5, 15, 25, 35, 45, 55, 65, 75, 85, 90
Orog_2019W2	45° 03'50.8"	100° 34'50.6"	Orog (west)	14 Feb. 2019	90	100*	5, 15, 35, 55, 75, 90

**Table A3. Solution chemistry of lake bottom-waters collected from Olgoy and Orog lakes in January 2020.**

\*The saturation index (SI) was obtained at 0°C.

Property	Olgoy_2020C1 lake water	Olgoy_2020C2 lake water	Orog_2020W1 lake water	Orog_2020C1 lake water	Orog_2020C2 lake water	Orog_2020C3 lake water
Na (ppm)	1,788	1,725	10,225	2,219	1,562	1,800
K (ppm)	22	22	485	24	20	21
Mg (ppm)	671	650	1,596	318	226	245
Ca (ppm)	12	11	55	33	36	36
Cl (ppm)	977	961	8,510	2,139	1,323	1,602
SO <sub>4</sub> (ppm)	1,487	1,458	7,063	1,460	972	1,085
Salinity (ppm)	4,957	4,827	27,934	6,193	4,139	4,789
pH	9.2	9.1	8.2	8.6	8.7	8.6
Alkalinity (mEq/L)	77.43	73.43	201.54	44.72	32.94	37.1
EC (mS/m)	967	1049	4380	1173	876	1004
DO (mg/L)	17.99	13.15	0.1	0.11	0.09	0.1
ORP (mV)	-268	-272	101	71	76	83
Temperature (°C)	-0.4	-0.2	-1.3	-0.2	-0.3	-0.1
Saturation index (SI) of calcite**	1.237	1.192	1.316	1.165	1.192	1.089
SI of magnesite**	2.673	2.606	2.393	1.599	2.606	1.54
SI of dolomite**	4.205	4.092	4.003	3.058	4.092	2.923
SI MHC (CaCO <sub>3</sub> .H <sub>2</sub> O)**	0.581	0.399	0.385	0.348	0.492	0.368
SI AMC (MgCO <sub>3</sub> .nH <sub>2</sub> O)**	0.215	0.147	-0.333	-0.831	-0.869	-0.966

**Table A4. Minerals, dissolved species, and gas species considered in the model calculations using FREZCHEM.**

\* The number of water hydrations (n) in amorphous Mg-carbonate was assumed to be three in our calculations (e.g., White et al., 2014).

Solid species	H <sub>2</sub> O(cr), NaCl·2H <sub>2</sub> O, Na <sub>2</sub> SO <sub>4</sub> ·10H <sub>2</sub> O, Na <sub>2</sub> CO <sub>3</sub> ·10H <sub>2</sub> O, NaHCO <sub>3</sub> , CaCO <sub>3</sub> (calcite), CaCO <sub>3</sub> (aragonite), CaCO <sub>3</sub> ·H <sub>2</sub> O (MHC), MgCO <sub>3</sub> (magnesite), MgCO <sub>3</sub> ·nH <sub>2</sub> O* (amorphous Mg-carbonate), CaMg(CO <sub>3</sub> ) <sub>2</sub>
Aqueous species	H <sub>2</sub> O(l), Na <sup>+</sup> , K <sup>+</sup> , Mg <sup>2+</sup> , Mg(OH) <sup>+</sup> , Ca <sup>2+</sup> , H <sup>+</sup> , Cl <sup>-</sup> , SO <sub>4</sub> <sup>2-</sup> , HCO <sub>3</sub> <sup>-</sup> , CO <sub>3</sub> <sup>2-</sup> , OH <sup>-</sup> , CO <sub>2</sub> (aq), CaCO <sub>3</sub> (aq), MgCO <sub>3</sub> (aq)
Gaseous species	H <sub>2</sub> O(g), CO <sub>2</sub> (g)

### References for Appendix A

Takahashi, Y., Miyoshi, T., Yabuki, S., Inada, Y., & Shimizu, H. (2008). Observation of transformation of calcite to gypsum in mineral aerosols by Ca K-edge X-ray absorption near-edge structure (XANES). *Atmospheric Environment*, 42(26), 6535–6541. doi:10.1016/j.atmosenv.2008.04.012

White, C. E., Henson, N. J., Daemen, L. L., Hartl, M., & Page, K. (2014). Uncovering the true atomic structure of disordered materials: the structure of a hydrated amorphous magnesium carbonate (MgCO<sub>3</sub>·3D<sub>2</sub>O). *Chemistry of Materials*, 26, 2693–2702. doi:10.1021/cm500470g